SUMMARY OF SICENTIFIC ACHIEVEMENTS

1. Applicant names and surname: **Iwona Maria Gorczynska**

2. Diplomas and scientific degrees with listed year, name of the received scientific degree, name of the granting institution, title of the doctoral dissertation.

- **2006 doctoral degree in physics**, Institute of Physics, Nicolaus Copernicus University, Torun, Poland
  Title of the doctoral dissertation: ”Imaging resolution in spectral domain optical coherence tomography”, supervisor: prof. dr hab. Piotr Targowski
- **2001 master of science degree in physics**, Faculty of Physics, Astronomy and Informatics, Nicolaus Copernicus University, Torun, Poland
  Title of the thesis: ”Speckle phenomenon and its selected applications”,
  supervisor: prof. dr hab. Piotr Targowski

3. Employment in scientific and research institutions.

2014 – 2017 Department of Ophthalmology and Vision Science, University of California in Davis, Sacramento, CA, USA, position: visiting assistant professor.

2009 – 2018 Faculty of Physics, Astronomy and Informatics, Nicolaus Copernicus University, Torun, Poland, position: assistant professor.

2006 – 2008 Research Laboratory of Electronics, Massachusetts Institute of Technology, Cambridge, MA, USA and Tufts – New England Medical Center, Boston, MA, USA (joint position), position: visiting scientist.

2006 – 2009 Faculty of Physics, Astronomy and Informatics, Nicolaus Copernicus University, Torun, Poland, position: university assistant.

4. Indication of the scientific achievement according to article 16, paragraph 2, “Degrees and titles in sciences and arts” act from March 14th 2003 (Dz. U. 2016 r. poz. 882 ze zm. w Dz. U. z 2016 r. poz. 1311).

a. Title of the scientific achievement

Development of experimental methods for high speed optical coherence tomography imaging and applications in examination of the human retinal tissue morphology, and posterior eye segment vascular networks.

b. List of scientific works selected for presentation of the scientific achievements

Numbering consistent with appendix 4.
Authorship statements are included in appendix 4.
Sums of the times the publications were cited are given according to Web of Science.

I.B.1. I. Gorczynska, J. V. Migacz, R. J. Zawadzki, A. G. Capps, J. S. Werner, "Comparison of amplitude-decorrelation, speckle-variance and phase-variance OCT angiography methods for imaging the human retina and choroid," Biomedical Optics Express **7**(3), 911-942 (2016).
https://doi.org/10.1364/BOE.7.000911 (open access)
Impact factor in the year of publication: 3.344, sum of the times cited: 13

I.B.2. M. Szkulmowski, I. Gorczynska, D. Szlag, M. Sylwestrzak, A. Kowalczyk, M. Wojtkowski, "Efficient reduction of speckle noise in Optical Coherence Tomography," Optics Express **20**(2), 1337-1359 (2012). https://doi.org/10.1364/OE.20.001337 (open access)

Impact factor in the year of publication: 3.546, sum of the times cited: 48

I.B.3. I. Grulkowski, I. Gorczynska, M. Szkulmowski, D. Szlag, A. Szkulmowska, R. A. Leitgeb, A. Kowalczyk, M. Wojtkowski, "Scanning protocols dedicated to smart velocity ranging in Spectral OCT," Optics Express **17**(26), 23736-23754 (2009).
https://doi.org/10.1364/OE.17.023736 (open access)

Impact factor in the year of publication: 3,278, sum of the times cited: 69

I.B.4. I. Gorczynska, V. J. Srinivasan, L. N. Vuong, R. W. S. Chen, J. J. Liu, E. Reichel, M. Wojtkowski, J. S. Schuman, J. S. Duker, J. G. Fujimoto, "Projection OCT fundus imaging for visualizing outer retinal pathology in non-exudative age related macular degeneration," British Journal of Ophthalmology, bjo.2007.136101 (2009).
http://dx.doi.org/10.1136/bjo.2007.136101

Impact factor in the year of publication: 2,917, sum of the times cited: 32

I.B.5. B. Potsaid, I. Gorczynska, V. J. Srinivasan, Y. Chen, J. Jiang, A. Cable, J. G. Fujimoto, "Ultrahigh speed Spectral / Fourierdomain OCT ophthalmic imaging at 70,000 to 312,500 axial scans per second," Optics Express **16**(19), 15149-15169 (2008).
https://doi.org/10.1364/OE.16.015149 (open access)

Impact factor in the year of publication: 3,880, sum of the times cited : 227

- Citations of the publications selected for the scientific achievement presentation: 389
- Citation of all applicant's publications: 1667
- Hirsch index (h-index): 21

c. Description of the scientific goals, accomplishments and applications

4.1. SUBJECT AND AIMS OF THE SCIENTIFIC WORK, AND APPLICATIONS OF THE RESULTS

The topic of my scientific work was development of experimental methods for Fourier-domain optical coherence tomography (FdOCT) to enable fast, three-dimensional imaging of the human posterior eye segment, including imaging of the tissue and vascular morphology, and blood flow velocity measurement in the retinal and choroidal vessels. The aims were to design and construct imaging setups, develop experimental, data processing and visualization methods to enable qualitative and quantitative analysis of normal eyes and eyes affected by retinal pathology. The imaging setups and methods were used for patients imaging in the ophthalmology clinics and commercialized in a form of know-how transfer to industry.

4.2. RESEARCH MOTIVATION

Optical coherence tomography (OCT) is a set of three-dimensional imaging techniques extensively developed by research groups around the world for the last 25 years. One of its most successful applications is in ophthalmology. Since the first publications reporting OCT imaging of the eye [1-3], there is a growing interest in development of methods for ophthalmology research and to enable diagnostics and monitoring of the eye diseases development and treatmet [4]. However, despite the progress

in research on advanced methods for imaging and analysis of tissue functioning [5-16], blood circulation in vascular networks [17-35], examination of tissue spectoscopic properties [36-43], and for quantitative data analysis [44-65], the majority of clinical applications utilize qualitative assessment of tissue morphology in OCT images. In the past ten years, there has been a rapid advancement in imaging of the posterior eye segment vasculature – OCT angiography methods have been invented and commercialized [66-89]. Yet, most of the published clinical applications rely on qualitative evaluation of the vascular structural images. The disconnection between the development of advanced methods for tissue and vascular networks morphology and function analysis, and their applications in clinical ophthalmic diagnostics arises *i.a.*, from the complexity of the experimental setups and methods, requirement for the use of advanced data analysis methods, and difficulties in the results interpretation due to presence of various confounding factors. One of the origins of these challenges is insufficient imaging speed.

The goal of my research was experimental demonstration that increasing imaging speed in Fourier domain OCT not only improves the quality of the acquired data and facilitates easier qualitative and quantitative analysis of tissue morphology, but also enables development of uncomplicated experimental methods for clinical applications. It provides detailed information about vascular networks of the posterior eye segment down to the capillary vessels and allows to develop methods for quantitative analysis of vascular morphology and for measurement of blood flow velocity. The far-reaching goal of my research is to develop experimental and numerical data processing methods for modeling of blood flow in the three-dimensional network of retinal vessels and two-dimensional meshwork of *choriocapillaris*. In the future, such methods may enable better understanding of the tissue perfusion mechanisms and blood circulation in the retinal and choroidal vasculature.

4.3. THE OUTLINE OF THE RESEARCH ACHIEVEMENTS SUMMARY

The summary of my scientific achievements begins with an outline of the optical coherence tomography principles and introduction of the terminology used for its description. Scientific projects constituting the achievement are summarized in the section “Realization of the research projects”. My research consisted of a few stages: design, construction and tests of the experimental setups, design and realization of the experiments, development and implementation of data analysis methods. The description of my work is divided into three sections, within which a chronological order is preserved: “Design and construction of experimental setups”, “Development of experimental methods for high speed OCT imaging”, “Numerical data analysis”. The summary finishes with a “Recapitulation” section.

4.4. INTRODUCTION

The term optical coherence tomography (OCT) describes a wide range of methods developed for imaging objects semi-transparent for visible light and near infrared radiation (~800 nm – 1500 nm). The fundamental physical phenomenon used in OCT imaging is interference of low temporal coherence light. If a light of low temporal coherence is used in an interferometry setup, *e.g.* in a Michelson interferometer, the interference fringe pattern will be observed only for a narrow range of optical path differences between the arms of the interferometer. The shorter is coherence time, *i.e.* the broader is the spectral bandwidth of the light, the shorter is the range of optical path differences for which the fringe pattern can be observed, *i.e.* the lengths of the interferometer arms can be equalized with a higher

precision. If one of the arms contains an object composed of a set of layers differing in the refractive index value, then light back-scattered at the layers' boundaries will give rise to interference fringes. The fringe pattern can be used to obtain information about the optical distances between the boundaries. The shorter is the coherence time of light, the shorter is the distance between the layers which can be unambiguously resolved, i.e. the better is the resolution of the measurement.

One of the criteria used for classification of OCT techniques is the method of interference signal detection. The fringe pattern can be registered over time, during the change of the reference arm length. Equalizing the length of the reference arm with the length of the sample arm, up to the selected layer inside the object, will generate an interference fringe. Its visibility (measured *e.g.* as a Michelson contrast) increases with decreased lengths mismatch. The location of the layer corresponds to the length of the reference arm for which a maximum fringe visibility is registered. The locations of the subsequent layers are detected as consecutive maxima during the change of the reference arm length. This interference signal detection method gave rise to the time-domain optical coherence tomography (tdOCT) technique [1].

The interference signal can be also observed in the spectrum of light. In this realization of the experiment, the reference arm length of the interferometer is matched to the location of the object in the sample arm (it is usually slightly shorter or slightly longer) and remains constant during the imaging. If the optical path difference is an integer multiple of the wavelength for a given spectral component, then the receiver will detect a maximum light intensity corresponding to constructive interference. The same optical path difference may meet the condition of destructive interference for a different wavelength, and a minimum light intensity will be observed for that spectral component. The light intensity registered for consecutive wavelengths will oscillate between minimum and maximum forming a spectral fringe pattern. The frequency of the oscillations depends on the location of the scattering layers relatively to the position of the reference arm. The larger is the optical path difference, the higher is the frequency of the oscillations. The spectral interference pattern is a superposition of fringes with frequencies corresponding to locations of all scattering layers. Therefore, the analysis of frequency components in the registered signal provides information about the structure of the imaged object. Typically, the analysis is performed by Fourier transformation. This method of the interference signal detection is used in Fourier domain OCT (FdOCT) techniques, which can be further classified into spectral domain OCT (sdOCT) [2, 90-92] and swept source OCT modalities (ssOCT) [93-95]. In spectral domain OCT, the interference signal is registered with spectrometers. In swept source OCT, the fringe pattern is usually acquired by dual balanced photoreceivers (photodiodes) during a rapid wavelength sweep of the light emitted by the source.

In the FdOCT techniques, the three-dimensional data is typically obtained by scanning the object with a beam of light, with the use of optical scanners. Usually, raster scanning is implemented, in which the beam is deflected sequentially in two orthogonal directions: horizontal and vertical. Typically, fast scanning is performed in the horizontal direction. Spectral interference fringes acquired point-by-point along the fast scanning axis (A-scans) generate, after Fourier transformation, a two-dimensional cross-sectional image (B-scan). B-scans acquired sequentially along the slow scanning axis form a three-dimensional data set. In a basic, structural OCT imaging, the scanning density (number of A-scans per unit length of the object) is selected in such a way that the largest possible area of the object is imaged with no loss of information. *I.e*. the scanning step size is approximately equal to the half value of the transverse

imaging resolution. Data acquired in this manner can provide information about the morphology of the imaged tissue.

In addition to structural imaging, OCT techniques can enable detection of dynamic processes connected to the functioning of the biological tissues. One of such processes is blood flow in the vascular systems embedded in tissues. Two groups of blood flow imaging techniques are distinguished in optical coherence tomography: OCT velocimetry (OCT-V) and OCT angiography (OCTA).

OCT velocimetry techniques enable measurements of at least one of the velocity vector components. The measurement of the axial flow component (along the light propagation direction) is typically performed with Doppler OCT methods. The light back-reflected at the scattering centers moving within the object, experiences frequency shift due to the Doppler effect. Interference of this light with the reference beam creates "beating" of the light intensity observed in time. The description of the registered OCT signal (A-scan) affected by the Doppler effect can be performed with the use of power spectrum density function (*G*):

$$\begin{aligned} G(\omega) &= U_0^s(\omega)U_0^{s*}(\omega) + U_0^r(\omega)U_0^{r*}(\omega) + U_0^s(\omega)U_0^{r*}(\omega) + U_0^r(\omega)U_0^{s*}(\omega) \\ G(\omega) &= G_{ss}(\omega) + G_{rr}(\omega) + G_{sr}(\omega) + G_{rs}(\omega) \end{aligned}, \tag{1}$$

where:

$$U_0^x(\omega) = \alpha_x \int_{-T/2}^{T/2} u_0(t)\exp(-i\omega t)\,dt \tag{2}$$

describes one of the orthogonal polarization components of light propagating in the object (*x=s*) and reference arm (*x=r*) of the interferometer; *ω* – oscillation frequency of the electromagnetic wave, *T* – exposure time of the light receiver.

The interference terms in (1) can be represented by:

$$G_{sr}(k;t) = \alpha S(k)\exp(ik\cdot\Delta z)\exp\left(i\frac{4\pi V_z}{n\lambda}t\right), \tag{3}$$

with the use of a formula describing the Doppler frequency *ω"* of the light propagating in the optical medium with a speed c_m, and scattered by a scatterrer moving with the axial velocity V_z:

$$\omega'' = \omega\left(\frac{1-\frac{V_z}{c_m}}{\sqrt{1-\left(\frac{V_z}{c_m}\right)^2}}\right)^2 \cong \omega\left(1-2\frac{V_z}{c_m}\right), \tag{4}$$

k – wavenumber, *λ*- wavelength, *Δz* - optical path difference between the object and reference arm of the interferometer, *t* – running time, *α* – loss coefficient, *S(k)* – power spectrum density of light emitted by the source.

In Fourier domain OCT, the beating signal can be observed directly or indirectly. The direct measurement relies on the analysis of the beating frequency (*Ω*) which is typically performed by time-domain Fourier transformation (*FT*) followed by Fourier transformation in wavenumber domain [24, 96]:

$$G_{sr}(k;t) = \alpha S(k)\exp(ik\cdot\Delta z)\exp(i\Omega t) \tag{5}$$

$$\begin{aligned} g'_{sr}\left(k;V_z\right) &= FT(t)\left\{G_{sr}\left(k;t\right)\right\} \\ g_{sr}\left(z;V_z\right) &= FT(k)\left\{g'_{sr}\left(k;V_z\right)\right\} \end{aligned}, \tag{6}$$

where:
$$\Omega = \frac{4\pi}{n\lambda}V_z \rightarrow V_z = \Omega\frac{n\lambda}{4\pi} \tag{7}$$

is the beating frequency (or Doppler frequency) proportional to the flow speed. The larger is the axial flow velocity value, the larger is the frequency shift caused by the Doppler effect, and the larger is the beating frequency. The result of the two-dimensional Fourier transformation are: Doppler OCT A-scans enabling mapping of the axial flow velocity values in the depth of the imaged object, and structural A-scans used for the imaging of tissue morphology.

The indirect detection of the Doppler OCT signal relies on the analysis of the interference fringe pattern phase changes [17-19, 23, 97-100]. The phase of the interference fringe pattern is obtained by Fourier transformation in wavenumber domain of the registered OCT signal:

$$\begin{aligned} G_{sr}\left(k;t\right) &= \alpha S\left(k\right)\exp\left\{i\left[k\cdot\Delta z+\phi\left(t\right)\right]\right\} \\ g_{sr}\left(k;t\right) &= FT\left(k\right)\left\{G_{sr}\left(k;t\right)\right\} \end{aligned}, \tag{8}$$

where the phase of the fringe pattern: $\phi\left(t\right)=\frac{4\pi}{n\lambda}V_z t$ is a linear function of time. (9)

The OCT measurement of the transverse flow velocity vector component requires application of speckle field decorrelation rate analysis methods (decorrelation rate of the complex amplitudes obtained via Fourier transformation of the OCT signal) [84, 101, 102], Doppler signal broadening analysis methods [103-108], or application of multi-beam illumination methods [35].

OCT angiography [66] is a set of experimental and data analysis techniques enabling imaging of the vascular networks structure without the necessity to measure the blood flow velocity. Blood cells flowing through the beam of light introduce fluctuations to the complex amplitudes obtained by Fourier transformation of the registered interference fringe pattern. The fluctuations can be caused by the axial and transverse flow velocity components. To localize moving scattering centers within the static tissue volume, various metrics of the signal variability are defined. The most commonly used metrics are: amplitude variance (often called speckle variance) [69, 72], phase variance [70, 109], decorrelation of the real amplitude of the OCT signal [75, 77, 85], decorrelation of the complex amplitude [87, 89]. Large values of the signal variability metrics indicate locations of the moving blood cells, *i.e.* indicate locations of the vessels. OCT angiography can also use the Doppler OCT methods to visualize flow [67]. In this case, the quantitative information about flow velocity value is removed by calculating the power of the Doppler OCT signal (absolute value of the Doppler signal or its square) [78].

OCT velocimetry and OCT angiography techniques require analysis of the interference signals registered from the same location in the object. Therefore, the scanning should be performed in such a way that a set of A-scan is acquired from the same location in the object over a pre-defined period time. The most commonly used scan method meeting this requirement is a raster scan in which the scanning step is a few times smaller than the transverse imaging resolution (raster scan with a high oversampling). In the fast flow detection regime, the high oversampling is implemented in the fast scanning direction. In the slow flow detection regime, a set of scan methods is utilized including: acquisition of multiple B-scans (BM-scans) or volumetric data sets from the same position in the object, high oversampling in the slow scan direction, “back-stitch” scanning [76], or multi-beam scanning [110].

4.5. REALIZATION OF THE RESEARCH PROJECTS

The application of low temporal coherence light interference and Doppler effect for fast, three-dimensional, *in vivo* imaging of the posterior eye segment tissues and vascular systems required: design and construction of the OCT apparatuses, design of the experimental methods, development and implementation of data analysis and visualization methods, and performing experiments to demonstrate the applicability of the developed methods for imaging of healthy eyes and eyes affected by ocular pathologies. My research projects were realized in cooperation with:

- Medical Physics Group, Insititute of Physics, Nicolaus Copernicus University under the leadership of prof. A. Kowalczyk, where I was employed as a university assistant and assistant professor,
- Biomedical Optical Imaging and Biophotonics Group, Research Laboratory of Electronics, MIT, Cambridge, USA, under the leadership of prof. J.G. Fujimoto, where I completed a postdoctoral training (a joint appointment with the New England Eye Center, Tufts Medical Center, Boston, MA, USA),
- Vision Science and Advanced Retinal Imaging Laboratory, University of California, Davis Eye Center, Sacramento, USA, under the leadership of prof. J.S. Werner, where I have completed a senior scientific training as a visiting assistant professor.

4.5.1. DESIGN AND CONSTRUCTION OF THE EXPERIMENTAL SETUPS

The first stage of my research projects realization included design and construction of the experimental OCT setups for *in vivo* imaging of the human retina and choroid, which required recognition of the demands and limitations connected to: imaging of the living tissue, physical principles of the OCT technique, and available research equipment. In ophthalmic applications of the OCT technique, the two most important requirements are high imaging resolution and speed. The imaging resolution should enable detection of pathological changes developing in the retinal anatomical layers, *i.e.* it should not be lower than ~15 µm. The imaging speed should enable acquisition of diagnostically relevant data in less than 10 s (typically in ~5 s).

The transverse imaging resolution of optical imaging systems is determined by their numerical apertures. The higher is the numerical aperture, the higher is the transverse imaging resolution. However, in OCT technology, the optical setups designed for the imaging of the posterior eye segment include the optical apparatus of the eye itself. In this case, the imaging resolution is no longer limited by the numerical aperture of the optical system but by the aberrations of the eye. In the classic OCT imaging systems utilizing Gaussian beam optics, the transverse imaging resolution can reach ~7-10 µm in the eyes of volunteers with good visual acuity. Achieving higher imaging resolutions requires application of adaptive optics techniques correcting aberrations of the eye.

The axial imaging resolution in OCT techniques depends on the spectral bandwidth of the light emitted by the source. Application of near infrared light (~750 – 1100 nm) with a broad spectrum (~80-100 nm), enables axial imaging resolution of ~3-8 µm. However, the broader is the light spectrum, the more difficult becomes the detection of the interference signal in spectral domain OCT, and the more difficult is construction of the light sources for the swept source OCT technique. In both cases, it is necessary to control and compensate the dispersion of light in the optical elements and in the eye, and to control the polarization of light propagating in the optical fibers (polarization modes). In addition, the design and construction of the spectrometers enabling high axial imaging resolution (a few microns),

large imaging depth (~1-1.5 mm with sensitivity roll-off below ~19 dB) and high imaging speed (A-scan rate of ~ 100-300 kHz) becomes challenging in sdOCT.

The imaging speed is one of the most important specifications of the OCT apparatuses designed for the imaging of the human eye *in vivo*. The higher is the imaging speed, the larger area of the object can be scanned, and the more information can be obtained from a single data set. However, acquisition time of a single data set is usually limited to ~5 s, to avoid involuntary eye motion and drying of the tear film. The attempt to increase the imaging time in order to acquire more data, results in increased number of motion artifacts and degradation of the image quality. One solution of this problem is application of active (in the real time) or passive (in post-processing) eye tracking methods, described later in this research summary. Even though they do not eliminate the eye motions, they can correct artifacts caused by the motion.

Regardless of the possibility to apply motion correction methods in connection with the OCT technique, it is desirable to increase the speed of the OCT imaging itself. It not only enables to increase the scanned object area but is also essential in the development of methods for monitoring dynamic processes over time, for example detection of the blood flow in the vascular networks. However, the consequence of the increased imaging speed is decreased imaging sensitivity. The exposure of the eye to near infrared radiation is limited by the safety norms. In OCT setups utilizing light with the center wavelength of ~850 nm (typical for spectral domain OCT), the power of light which can be used for retinal imaging is limited to ~800 μW. In OCT systems utilizing sources emitting light at the center wavelength of ~1050 nm (typical for swept source OCT), the light power is limited to ~1.8 mW. Increasing the imaging speed without the possibility to increase the light power results in a decreased number of photons received by the photodetector in a single exposure and, in consequence, in a drop of the imaging sensitivity. On the other hand, more data can be acquired enabling application of OCT signal averaging techniques and providing larger amount of diagnostically relevant information. Determination of the imaging speed limit above which no new information about tissue morphology or function can be obtained in the imaging of the posterior eye segment, is a subject of an on-going scientific debates. In my research projects, I was experimentally demonstrating what new information about tissue morphology, vascular morphology, and blood flow can be obtained by increasing the imaging speed in Fourier domain OCT techniques.

In the design of the OCT apparatuses for the imaging of the posterior segment of the eye [I.B.1-5], I have utilized classic Gaussian beam optics solutions. This choice was dictated by the objectives of the research projects to image retinal tissues and the choroid with resolution enabling identification of anatomical layers but without the need to image individual retinal cells. For the construction of the interferometers, I have utilized single mode, polarization insensitive fiber optics elements. The application of fiber optics was necessary to minimize the influence of the environmental conditions on the registered interference signals and to enable the use of OCT apparatuses in the ophthalmology clinics. The selection of single mode optical fibers was necessary to avoid modal dispersion and to enable detection of the interference signal. The selection of polarization insensitive optical elements was dictated by the need to avoid dispersion and polarization effects in the acquired OCT images (attenuation of the interference signal in the birefringent tissues and introducing optical delays between the polarization modes of light propagating in the fibers) without the necessity to precisely control the polarization state of light. For the construction of the OCT setups I utilized sources emitting near

infrared light: commercially available superluminescent diodes, femtosecond lasers [I.B.2-4], and swept source lasers [I.B.1], as well as light sources constructed in research laboratories for the OCT imaging (femtosecond lasers [I.B.5], supercontinuum generated in the photonics crystal fibers [II.A.22]). In spectral domain OCT, utilization of light sources with various spectral bandwidths required customizing the design of the spectrometers, to enable high speed detection of the interference signals [I.B.2-5]. For the construction of the spectrometers, I utilized optical elements enabling sufficient spectral resolution (polarization insensitive, holographic transmission diffraction gratings, objectives corrected for chromatic and geometric aberrations) and cameras enabling sufficient imaging speed (line-scan CCD and CMOS cameras).

4.5.2. DEVELOPMENT OF EXPERIMENTAL METHODS FOR HIGH SPEED OCT IMAGING

My early research projects on development of high speed OCT techniques included design of the experimental setups and methods, and development of visualization methods for three-dimensional OCT data in spectral domain OCT [I.B.4, II.A.12, II.A.14, II.A.16, II.A.19-27]. Available at that time line-scan CCD cameras enabled imaging with speeds of ~25 000 A-scans/s. During a 5 s imaging time, it was possible to acquire a data set consisting of ~350 x 350 x 2048 pixels, sufficient for three-dimensional visualization of retinal tissue morphology with ~15 µm transverse, and ~3-5 µm axial resolution, in the eyes of heathy volunteers and in subjects with retinal pathologies [I.B.4, II.A.7, II.A.16, II.A.26, II.B.23 - 25, II.B.27]. However, the new imaging possibilities also generated new challenges. The diagnostic usefulness of the three-dimensional data sets depends not only on the details of the imaged pathological changes but also on the possibility of their visualization in a way easy to interpret by the ophthalmologists. The development of methods for visualization of three-dimensional data obtained in high speed OCT imaging was one of the objectives of my postdoctoral training. The project resulted in demonstration of a method for visualization of the outer retinal pathology in the age related macular degeneration (AMD), in a form of *en face* projections of selected retinal layers (Fig.1.) [I.B.4]. The summary of the data processing methods is presented in the section “Numerical data analysis”. The results of the project were presented *i.a.* at Photonics West, BiOS, Ophthalmic Technologies 2007 conference, where my presentation was nominated for the Pascal Rol Award. The nominations are a recognition of the authors of the top fife submissions, as scored by the reviewers committee.

Although the early research on development of spectral domain OCT demonstrated the possibility of three-dimensional imaging of the tissue morphology, three-dimensional imaging of the vasculature and measurement of blood flow velocities required an increase of the imaging speed. This was also one of the objectives of my postdoctoral training. The main goal of my research was development of sdOCT setups and experimental methods with the use of line-scan CMOS cameras [I.B.5]. The experiments demonstrated that high imaging speeds require achieving compromises between a set of imaging parameters: sensitivity, axial resolution, imaging depth, scanning range. The possibility to image human retina with 70 kHz – 300 kHz A-scan rates, ~90-94 dB sensitivity and ~3-9 µm axial imaging resolution was demonstrated in the eyes of healthy volunteers. The increased imaging speed enabled acquisition of three-dimensional data sets consisting of 512x512x800 pixels in ~1.3 s. Shortening of the imaging time decreased the influence of eye motion on the image quality, enabled three-dimensional tracking of the eye movements in time and correction of the motion artifacts in the acquired data sets (Fig.2.). The decrease of motion induced image distortions and high transverse imaging resolution (~10 µm) enabled

visualization of individual cone photoreceptor cells at selected eccentricities from the fovea (>~4°) of a normal eye, without application of adaptive optics techniques (Fig.2g). Presentation of the results of this project at Photonics West, BiOS, Ophthalmic Technologies 2009 conference was nominated for the Pascal Rol Award.

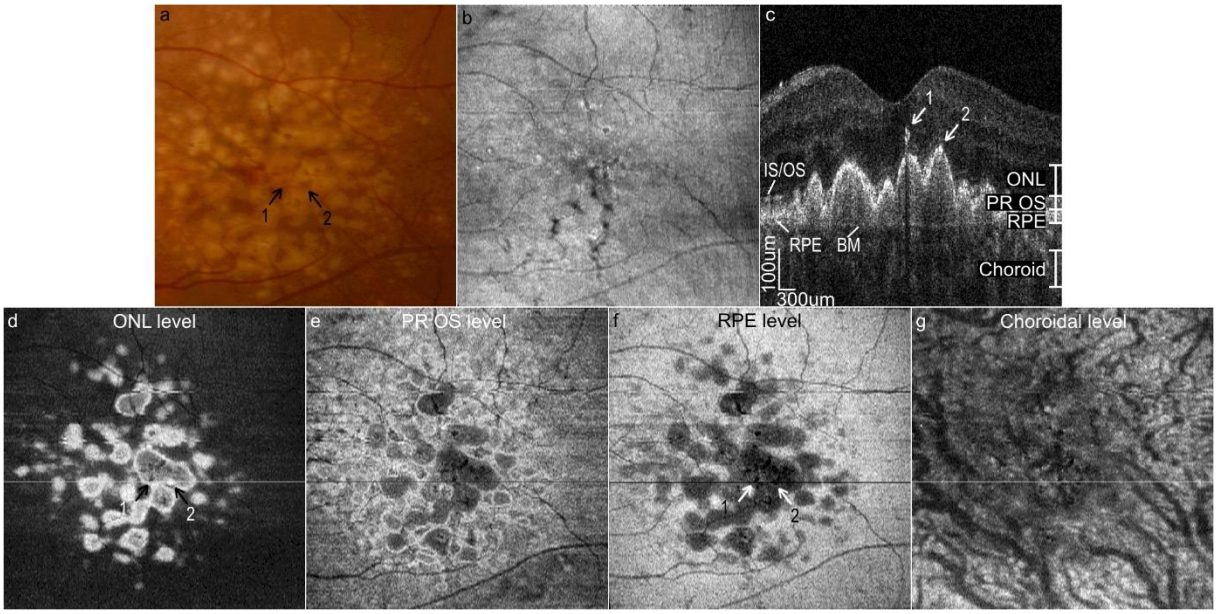

Fig. 1. Visualization of three-dimensional structural sdOCT data in *en face* projection images from selected depth layers. Case: age related macular degeneration, soft, confluent drusen. (a) Color fundus photograph. Arrows 1 and 2 indicate pigmentary changes. (b) OCT fundus image. (c) Example cross-sectional OCT image extracted from the 3-D data set. Arrow 1 shows pigment migration, and arrow 2 shows pigment accumulation. (d–g) Projection OCT fundus image at the levels shown in (c). The location of the cross-sectional OCT image (c) is shown as a line on the projection OCT fundus images. BM – Bruch's membrane; ELM - external limiting membrane; IS/OS - photoreceptor inner/outer segment junction; ONL - outer nuclear layer; PR OS - photoreceptor outer segments layer; RPE - retinal pigment epithelium. Image sizes are 6 mm x 6 mm.

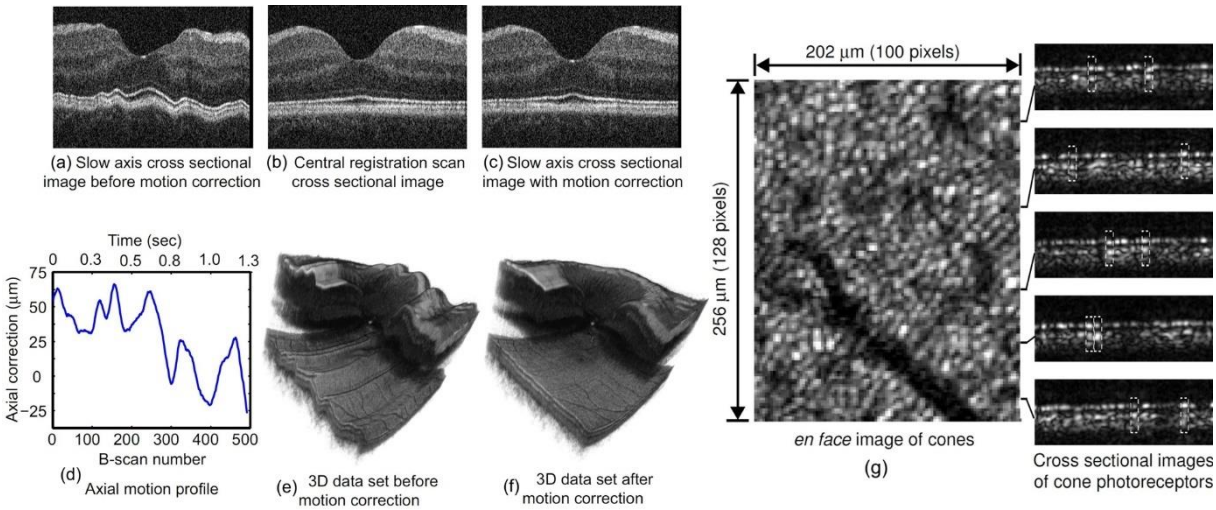

Fig.2. Application of spectral domain OCT system operating at 300 000 A-scans/s for eye motion artifacts correction (a - f) and visualization of the photoreceptor cells.

Perhaps the most important consequence of the increased imaging speed was the possibility to observe dynamic processes connected to the functioning of the living tissue, in particular the prospect to detect the blood flow in the retinal vasculature in volumetric data sets. The capability of sdOCT systems

of high speed retinal imaging was a basis for my further research on development of experimental methods for detection and measurement of blood flow in the retinal vasculature, down to the level of capillary vessels [I.B.2, I.B.3, II.B.8, II.B.10, II.B.11, II.B.15, II.B.16]. The research projects were conducted during my employment as a university assistant and assistant professor at Institute of Physics, Nicolaus Copernicus University, Poland.

The detection of blood flow in the retinal vessels requires acquisition of a collection of OCT A-scans from the same position in the imaged object, and in time intervals enabling observation of the signal changes caused by the moving blood cells. In standard experimental methods, the retina is imaged with the use of raster scans, in which the scan step in the fast scanning direction is several times smaller than the transverse imaging resolution (high oversampling in the fast scanning direction). This provides several (~5-15) data points (A-scans) from each position in the object, and enables detection and measurement of the blood flow with the use of OCT velocimetry methods. However, this scanning method limits the range of flow velocity values which can be unambiguously measured with a given OCT setup. The upper limit for the flow velocity measurement is set by the imaging speed. The higher is the imaging speed, the higher flow velocity can be measured. The lower velocity limit is set by the presence of noise in the acquired complex OCT signals. If the signal change caused by the flow is smaller than the noise level, detection and velocity measurement of such flow is not possible. In my research, I was focusing on development of methods for slow flows detection and measurement (below the limits of standard OCT scanning methods), preserving the capability of fast flow velocity measurements and the capability of three-dimensional imaging [I.B.2, I.B.3, II.B.10, II.B.11, II.B.15, II.B.16]. The foundation of these projects was an extremely simple observation that detection of slow flows requires increasing the time interval between acquisitions of subsequent A-scans, used for OCT velocimetry computations. Although this approach does not decrease the noise level, it allows for larger (observable) change of the complex OCT signal between subsequent acquisitions. Paradoxically, increasing the imaging speed was critical to achieve this goal. Fast data acquisition enabled implementation of scan protocols in which the scan step along the slow scanning direction (typically vertical) is several times smaller than the axial imaging resolution (oversampling in the slow scanning direction). The flow analysis is then performed among subsequent B-scans, in time intervals a few hundred times longer than given by the imaging speed of the OCT apparatus (multiple of the number of A-scans per B-scan). Despite the simplicity of this concept, its experimental realization was not trivial. It required achieving a set of compromises influencing the noise level, number of imaging artefacts, accuracy of the images, scanned area, total imaging time, sensitivity to specific flow velocity ranges. Application of this method in an OCT system operating at 200 kHz A-scan rate enabled detection of flows with axial velocity values of ~0.1 mm/s, in the 1 mm^2 area of the retina, and facilitated three-dimensional OCT angiography imaging of the retinal capillary vessels (Fig.3.).

However, this method did not allow for the measurement of the flow velocity, since the velocities exceeded the upper limit given by the scan protocol (too long acquisition of the B-scans). The solution of this problem was an introduction of segmented scan protocols. To implement this idea, I have designed and constructed an OCT imaging system with application of an additional, resonant scanning device, which enabled segmented raster scanning [I.B.2, II.B.10, II.B.16]. This approach allowed to shorten the time interval between acquisitions of A-scans, sufficient to measure the axial blood flow velocity in selected retinal capillary vessels (upper velocity limit of 0.6 mm/s), with the application of Doppler OCT methods (Fig.5.). The same scanning protocol enabled measurement of the fast flow velocities (~40 mm/s) in larger

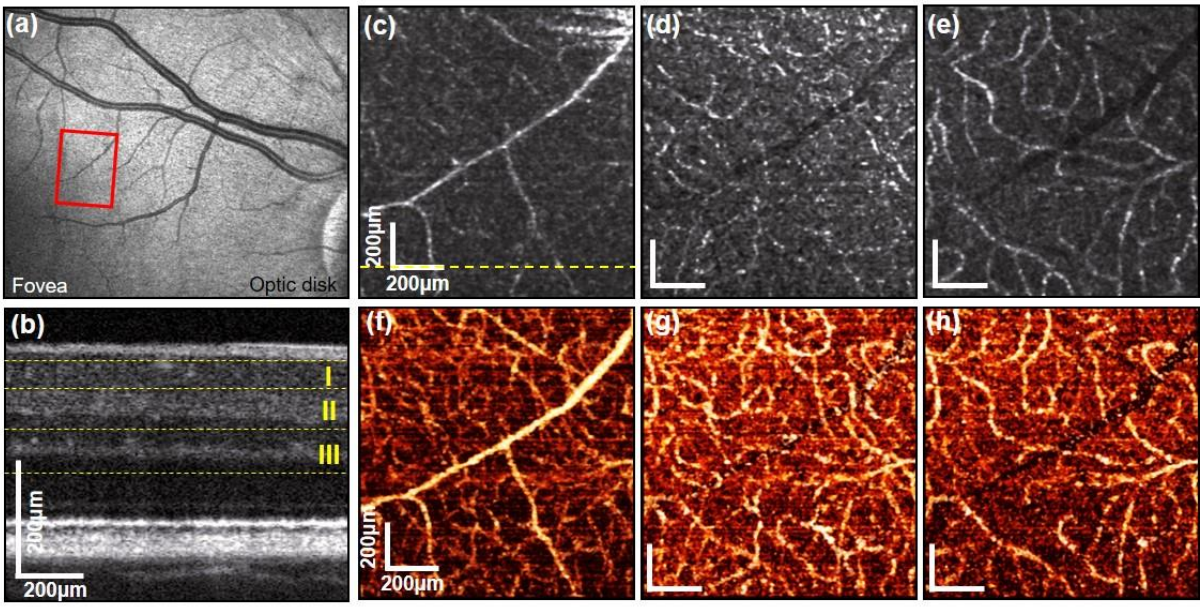

Fig.3. OCT angiography of the retinal vessels down to the capillary level. a. *En face* projection of three-dimensional OCT data set illustrating location of the area imaged with OCT angiography methods (rectangle). b. Example cross-sectional image indicating retinal vascular layers illustrated in c-h. c – e. Structural OCT *en face* projection images. f – g OCT angiography *en face* projection images. Images c – h were generated from the same data set with application OCT angiography data processing. I – inner retinal vessels layer illustrated in c, f. II – inner capillary layer illustrated in d, g. III – outer capillary layer illustrated in e, h.

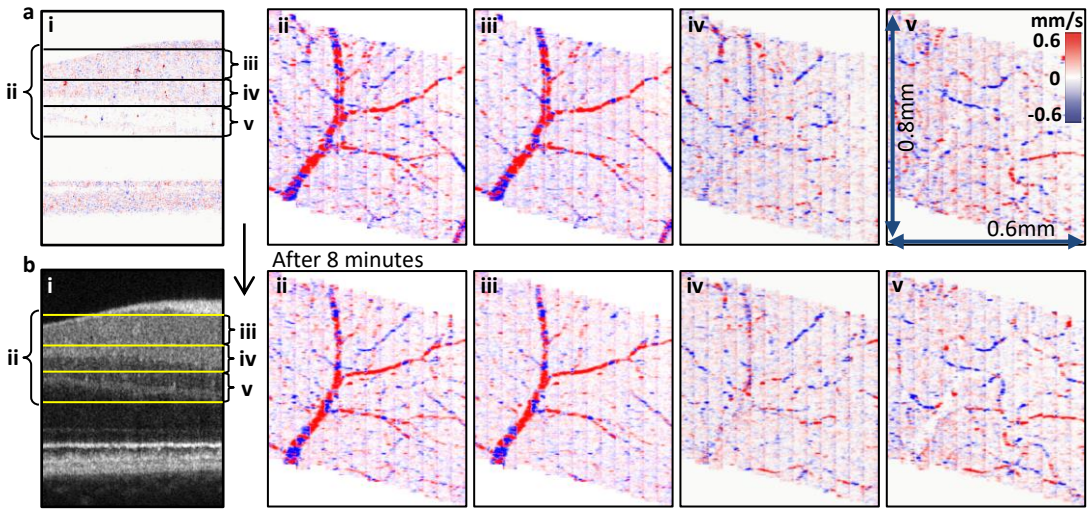

Fig.5. Blood flow velocity maps generated with joint spectral and time-domain OCT method. ii – v. *En face* projection images showing axial blood flow velocity component in the vessels located in retinal anatomical layers, indicated in cross sectional Doppler OCT image (ai) and structural OCT image (bi). ii. *En face* projection of the inner retinal layers. iii. Projections of the vasculature located in the ganglion cell layer. iv. Inner capillary plexus. v. Outer capillary plexus. Rows a and b show the same area in the retina imaged at time points separated by 8 minutes. Repeatable distribution of flow velocities is visible in each pair of the *en face* images.

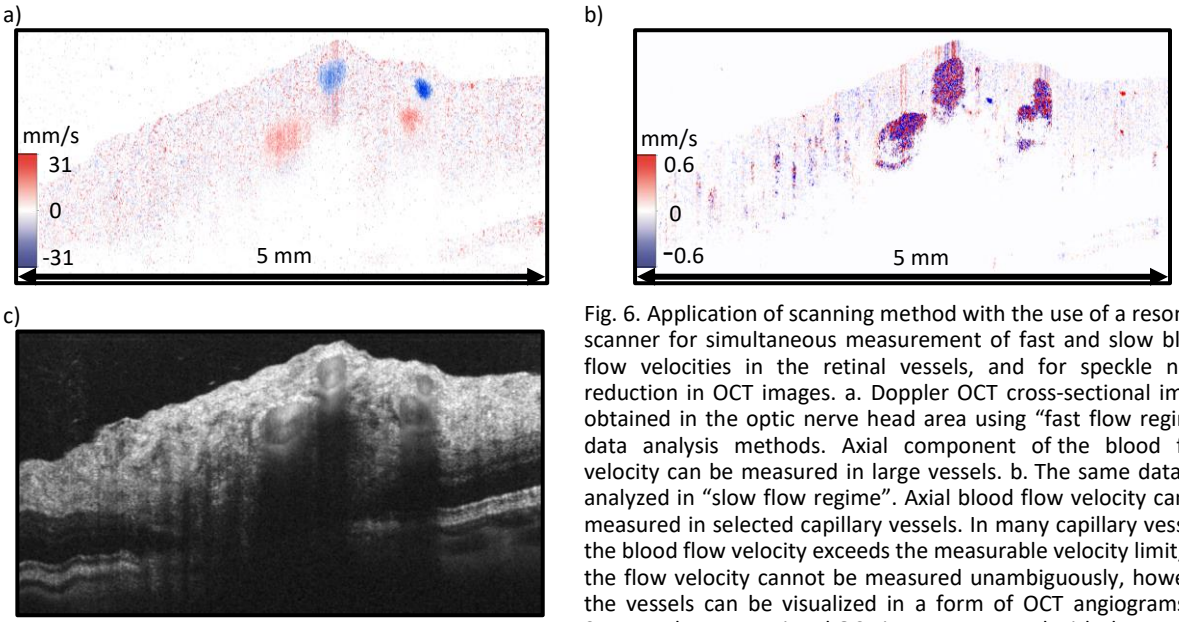

Fig. 6. Application of scanning method with the use of a resonant scanner for simultaneous measurement of fast and slow blood flow velocities in the retinal vessels, and for speckle noise reduction in OCT images. a. Doppler OCT cross-sectional image obtained in the optic nerve head area using "fast flow regime" data analysis methods. Axial component of the blood flow velocity can be measured in large vessels. b. The same data set analyzed in "slow flow regime". Axial blood flow velocity can be measured in selected capillary vessels. In many capillary vessels, the blood flow velocity exceeds the measurable velocity limit, *i.e.* the flow velocity cannot be measured unambiguously, however the vessels can be visualized in a form of OCT angiograms. c. Structural cross-sectional OCT image generated with the method for speckle reduction. All presented images were generated from the same data set.

vessels (Fig.6.). An additional advantage of the segmented raster scanning was implementation of data processing methods for suppression of the speckle noise [I.B.2].

For the realization of the summarized above research projects, I have used spectral domain OCT technique with application of sources emitting light at the center wavelength of ~850 nm, and CCD and CMOS cameras enabling imaging speeds from 25 000 A-scan/s to over 300 000 A-scans/s. The use of light at ~850 nm wavelength was not incidental. The near infrared radiation has sufficient depth penetration into the tissue to image all retinal anatomical layers. In the same time, the photosensitive elements used to manufacture the CCD and CMOS cameras have sufficient sensitivity at the near infrared wavelength range to detect the light back-reflected at all retinal layers. The combination of these two factors enabled development of methods for the imaging of the retinal vasculature. The next step in my research was development of methods enabling imaging of the choroidal vasculature of the human eye. The choroid is a densely packed, layered network of blood vessels located posterior to the retinal pigment epithelium (RPE), and isolated from the retina by the Bruch's membrane (blood-retinal barrier). The role of the choroid is to maintain the function of the photoreceptor cells by transporting substances involved in the visual processes and thermoregulation of the retinal tissues.

In the imaging of the choroid, it is advantageous to use light at a center wavelength of ~1050 nm, since the electromagnetic radiation at this wavelength has higher penetration through the retinal layers and the retinal pigment epithelium than light at ~850 nm. Imaging of the choroid at ~1050 nm center wavelength can be achieved by application of swept-source OCT techniques. Development of high speed swept source OCT imaging methods was one of the objectives of research projects which I have been conducting as a visiting assistant professor at University of California, Davis, USA. For the realization of the projects I have used commercially available wavelength-swept lasers operating at imaging speeds of 100 000 A-scans/s (100 kHz sweep repetition rate), and 1 700 000 A-scans/s (1.7 MHz sweep repetition rate).

In the first stage of the projects realization I have utilized a light source operating at 100 000 A-scans/s for the OCT angiography imaging of the human retina and choroid [I.B.1, II.B.5, II.H.1. II.H.8]. The experiments demonstrated the possibility of three-dimensional imaging of the retinal vasculature with details enabling application of semi-automatic data processing methods for vessels tracing. As a result, a skeletonized three-dimensional model of retinal vascular network was generated down to the level of the capillary vessels. It was the first demonstration of the possibility to model the morphology of the retinal vascular systems using OCT angiography techniques (Fig.7.). Data analysis methods based on the vessel tracing may enable modeling of the blood circulation and, in the future, better understanding the mechanisms of tissue perfusion.

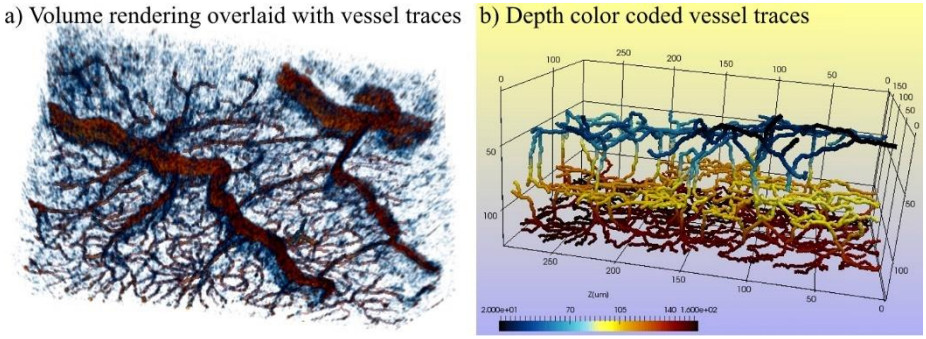

Fig.7. Results of user-guided retinal vessel tracing obtained with the Simple Neurite Tracker plugin of ImageJ [126] software and showcased with ParaVIEW software [127]. a) Volume rendering of the vessels overlaid with the vessel traces. b) 3D skeleton visualization of the traced vessels. Three vascular layers are visible: retinal vessels (blue), inner capillary plexus (yellow) and outer capillary plexus (red), as well as vessels connecting these layers. We have provided more detailed presentation of b) in https://dx.doi.org/10.6084/m9.figshare.2008674

One of the most important parts of the research project was a comparative analysis of a few most commonly used OCT angiography methods in imaging of the capillary vessels of the choroid (*choriocapillaris*) [I.B.1, II.B.5]. *Choriocapillaris* is a thin (~10 - 15 µm), highly perfused meshwork of vessels abutting the retinal pigment epithelium and Bruch's membrane. It is directly involved in the exchange of nutrients and waste materials of the phototransduction processes taking place in the photoreceptor layer, and therefore plays a critical function in the proper functioning of the photoreceptor cells. The role of the *choriocapillaris* in the development of neurodegenerative diseases, *e.g.* age related macular degeneration, is a subject of an on-going scientific debate. However, there is a lack of imaging methods which would enable detailed analysis of *choriocapillaris* morphology and function in the human eye *in vivo*. The classic ophthalmic diagnostic methods: indocyanine green angiography (ICGA) and fluorescein green angiography (FA), are used for the imaging of the choroid only in the suspicion of disease development in that layer (ICGA) or in case of exudative changes caused by retinal pathologies (FA). However, none of these methods enables to distinguish *choriocapillaris* from other choroidal layers (Sattler's and Haller's layer vessels). OCT angiography can offer this possibility. In my research, I have proposed methods for quantitative comparison of the *choriocapillaris* imaging contrast in OCTA. With their aid, I have demonstrated that although the most commonly used OCT angiography methods differ in the *choriocapillaris* imaging contrast, experimental and data processing methods have more significant influence on *choriocapillaris* visualization [I.B.1, II.H.1]. In particular, averaging of multiple volumetric data set significantly improves the imaging contrast of *choriocapillaris*. In OCT imaging techniques, averaging of multiple data set is not trivial because of the presence of various artifacts connected to involuntary eye

motion. It requires development of data processing methods enabling correction of the motion artifacts. Methods which I have used in realization of my projects are described in section "Numerical data analysis".

The application of swept source OCT setup at ~1050 nm center wavelength and 100 000 A-scans/s imaging speed enabled imaging of the *choriocapillaris* and small parts of larger choroidal vessels located directly underneath *choriocapillaris*. However, imaging of the larger vessels (Sattler's and Haller's layers) and obtaining information about blood flow velocity in these vessels was still not possible. Also, information about *choriocapillaris* morphology was still not attainable, *i.e.* it was not possible to propose any morphometric analysis of the *choriocapillaris* layer. Again, in my research projects, I have demonstrated that the solution of these problems is increased imaging speed in OCT techniques [II.B.4]. This project is connected to my current research conducted at Vision Science and Advanced Retinal Laboratory, University of Calfornia, Davis (in preparation for publication). I have presented its results at Photonics West, BiOS, Ophthalmic Technologies 2017 conference, at which my presentation was nominated to the Pascal Rol Award and recognized by the award committee as outstanding.

In my research projects, I have used a wavelength swept laser utilizing a Fourier domain mode locking (FDML) technique [II.B.19, II.B.20]. The laser operated at 1.7 MHz sweep rate (imaging speed of 1 700 000 A-scans/s), which is 17 times faster than imaging speeds offered by commercially available OCT angiography apparatuses. This light source enabled significant progress in imaging of the human choroid *in vivo*. I have experimentally demonstrated the possibility to image *choriocapillaris* layer down to its individual vessels, and to visualize deeper choroidal vessels. In addition, I have shown the possibility to obtain information about axial component of the blood flow velocity in selected choroidal vessels, with the application of Doppler OCT methods.

One of the outcomes of the project realization was demonstration that imaging of the *choriocapillaris* morphology is highly dependent on the scanning density [II.B.4]. It requires at least fulfilling the Nyquist criterion (scan step size should not exceed half of the transverse imaging resolution value). The smaller is the scan step, the better is the visualization of the *choriocapillaris* morphology (Fig.8.). However, decreasing the scan step below ~0.35 of the transverse resolution did not significantly improve the visualization of *choriocapillaris* structure. To enable quantitative assessment of the vascular structure visualization, I have developed a spatial power spectrum analysis of the *en face* projection OCTA images (summarized in the "Numerical data analysis" section).

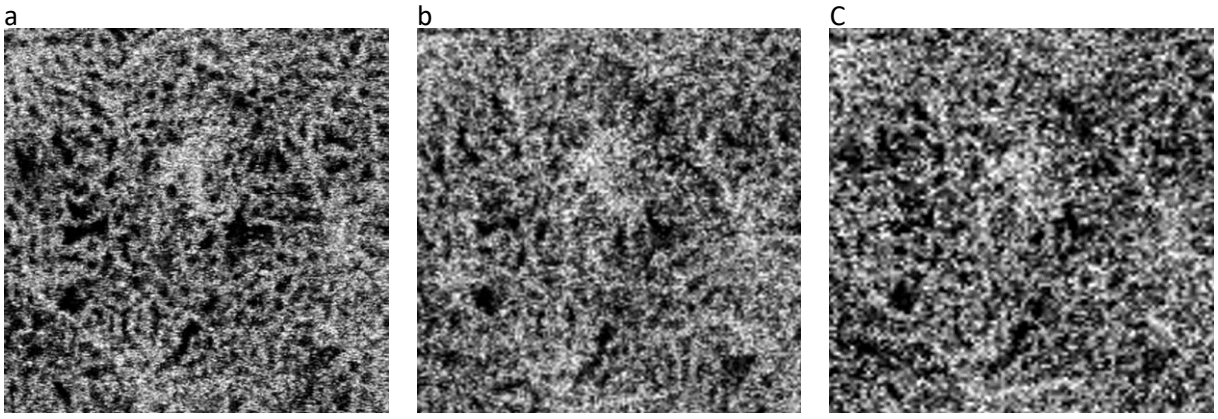

Fig. 8. Influence of scanning density on visualization of *choriocapillaris* in *en face* projections in FDML ssOCT angiography imaging. Scanning step sizes: a. 3 µm, b. 5 µm, c. 7 µm. The spot diameter of the imaging beam was 14 µm. With the increasing scanning step size, the quality of *choriocapillaris* visualization decreases. The projection images were generated from three different data sets acquired in the same area of a healthy eye. Image location: 3.5 deg nasally from the fovea. Image sizes: 0.8 mm^2.

Imaging rate of ~1.7 MHz enabled acquisition of three-dimensional data set consisting of 390x390x1024 pixels and covering ~1.2 mm^2 area of the object in ~2 s. To enable the detection of blood flow, B-scans were repeated 20 times at subsequent locations along the slow scanning direction, *i.e.* the total number of B-scans acquired in 2 s was 7800. The scanning step was 3 µm with the transverse imaging resolution of 14 µm. For comparison, acquisition of the same data set with commercially available OCTA devices would take ~30 s which is not acceptable in imaging of the human eye *in vivo*. The images obtained with this OCT setup and scan protocol had the level of details sufficient to develop methods for morphometric analysis of *choriocapillaris* [II.B.4]. I have proposed four metrics which can be used for quantitative assessment of the *choriocapillaris* in the eyes of healthy volunteers and in early stages of the outer retinal pathology development (*e.g.* in early stages of AMD): RPE-to-*choriocapillaris* distance, mean distance between vessels, spatial frequency bandwidth, flow fill factor (proportion of the flow area to the total imaged area) (Fig.11.-13.). Mapping of the RPE-to-*choriocapillaris* distances required development of numerical data processing methods for segmentation of the *choriocapillaris* layer and the retinal pigment epithelium. For the assessment of the inter-vessel distances and spatial frequency bandwidth, I have developed methods utilizing spatial power spectrum analysis. The estimation of the flow fill factor required application of morphological image analysis methods leading to binarization of the *choiriocapillaris* images.

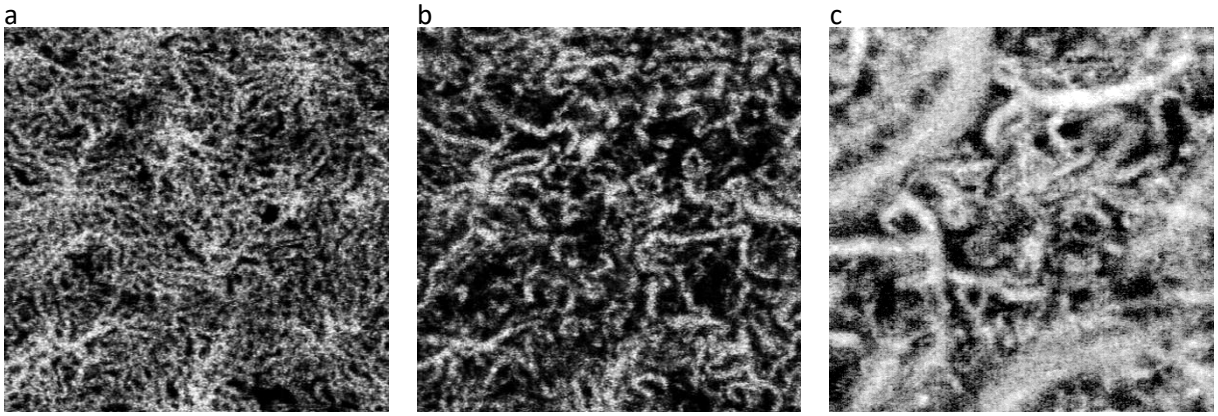

Fig.9. OCT angiography imaging of the human choroid *in vivo* with FDML ssOCT system at 1.7MHz A-scan rate. A. *En face* projection of the choriocapilllaris, visualized 16 µm below the RPE, layer thickness: 10 µm. b. Vessels localized 28 µm below the RPE, layer thickness 10 µm. c. Deep choroid: 90 µm below RPE, layer thickness: 98 µm. Images sizes: 1.22mm x 1.22 mm.

OCT angiography imaging at 1.7 MHz A-scan rate not only enabled visualization of the *choriocapillaris* layer, but also allowed for blood flow detection in deeper choroidal vessels (Sattler's and Haller's layers) (Fig.9.). This may seem counterintuitive because increased imaging speed results in a lesser number of photons registered by the photoreceiver in single exposure, *i.e.* decreases the imaging sensitivity. In addition, the deeper is the location of the imaged layers, the less light reaches those layers due to light scattering in the preceding tissues, and proportionally less photons reach the detector. Therefore, it may seem that increasing imaging speed should worsen the visualization of deep choroidal layers. However, increased imaging speed improves the visibility of the interference fringe pattern (decreased fringe wash-out caused by scanning, motion artefacts and mechanical instabilities of the imaging system), and enables acquisition of larger amount of data and application of signal averaging methods. These factors explain why, despite nearly twenty times higher imaging speed, it was possible to visualize deep choroidal vessels, which was not attainable before with the use of other

OCT imaging systems. Moreover, low phase noise of the light emitted by the FDML laser used in the imaging system, enabled detection of the Doppler signal generated by the blood flow in the deep choroidal vessels. Application of joint spectral and time-domain OCT method [24] resulted in measurement of the axial flow velocity component with values smaller than 0.4 mm/s (flow analysis was performed among B-scans, *i.e.* in the slow flow detection regime) (Fig.10.). Even more interestingly, application of fast flow detection data analysis revealed axial blood flow velocities in the order of 100 mm/s, originating form blood vessels most likely penetrating through the sclera and delivering blood to the choroid (probably short ciliary arteries). The most important consequence of the possibility to measure the axial flow velocity in choroidal vessels, is the chance to better understand the mechanisms of choroidal blood perfusion, and in the future, to model blood flow in the eyes of healthy volunteers and in subject with ocular diseases.

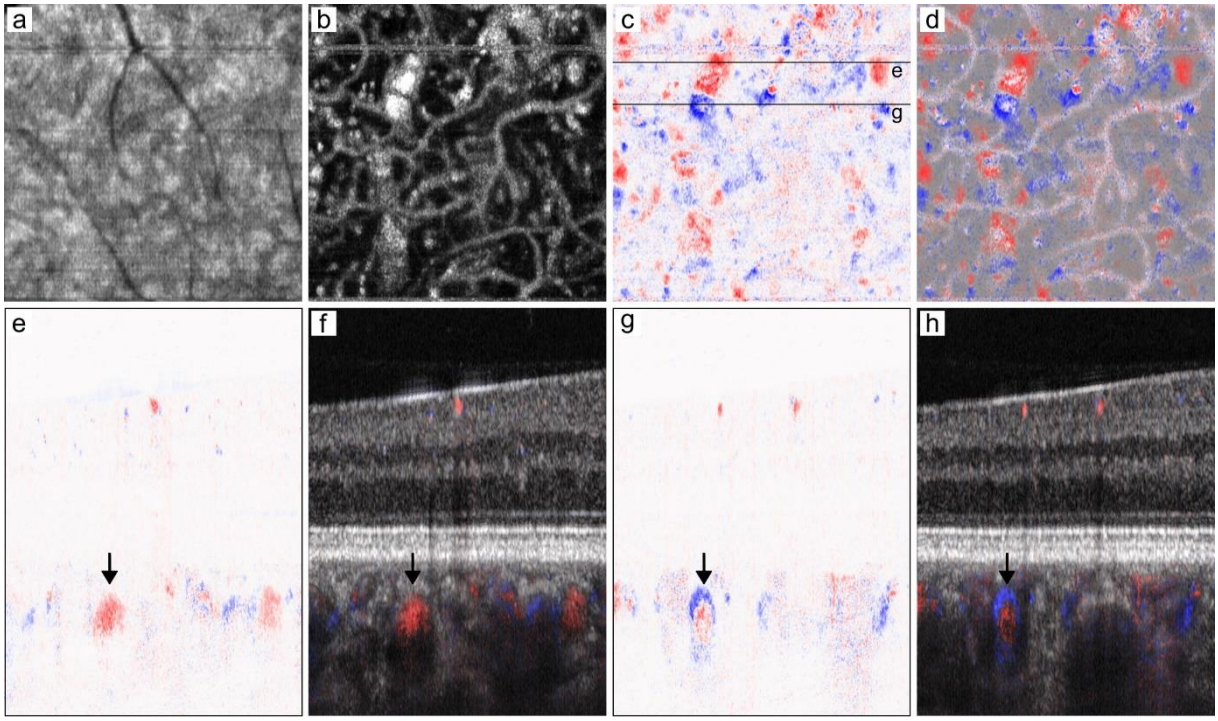

Fig. 10. OCTA and Doppler OCT images of the choroid in a healthy subject. a – intensity, b – OCTA, c – Doppler OCT *en face* projections. d. Overlay of the OCTA and Doppler OCT *en face* projections. e, g – Doppler OCT cross-sectional images. f, h – overlay of Doppler OCT cross-sections with intensity B-scans. Lines in image c indicate locations of the cross-sectional images shown in e and g. Arrows in e and f illustrate a vessel with Doppler signal originating from the inner part of a vessel. Arrows in g and h point at a vessel in which the axial velocity component moderately exceeds the maximum measurable velocity range generating rings of opposite colors. Red color in the Doppler OCT images indicates flow directions towards the RPE, blue – flow towards the sclera. Image location: 7 deg nasally from the fovea. Image sizes: 1.2mm x 1.2mm laterally, 787 µm axially.

4.5.3. NUMERICAL DATA ANALYSIS

Fourier domain OCT is an imaging technique largely relying on the numerical data analysis. The data processing methods used in OCT can be classified into several groups:

a) generation of images from the registered spectral interference signal,
b) visualization of features important in research problems analyzed with OCT,
c) qualitative and quantitative analysis of imaged objects features,
d) correction of artifacts caused by the deficiencies of the experimental methods.

An important part of my research projects was development of methods enabling visualization and quantitative analysis of selected morphological features of the human retina and choroid, and enabling correction of motion artifacts connected to involuntary eye motion.

a. Three-dimensional OCT data visualization methods.

OCT angiography and velocimetry imaging provides three-dimensional data sets. In scientific research and in clinical diagnostics, it is important to obtain information about object features hidden in the volumetric data sets. The posterior eye segment has a layered structure in which subsequent layers of cells play specific roles in the visual process. Similarly, the development of ocular diseases manifests in characteristic changes of selected anatomical layers. Intuitively, methods for three-dimensional data visualization should enable visualization of selected layers of the retina and choroid. My research focused on development of methods achieving this goal [I.B.1, I.B.4]. I have developed data analysis procedures relying on segmentation of a selected retinal layer mirroring the curvature of the normal eye fundus and generating a strong OCT signal. The remining retinal and choroidal layers are visualized relatively to this "reference layer" by axial summation of data at selected depth ranges. The requirements for the "reference layer" are met by the retinal pigment epithelium. For the segmentation of the RPE, *i.e.* for its automatic identification in the acquired B-scans, I have used gradient analysis methods, which enable edge detection of the features visualized in cross-sectional structural images. The main difficulty in direct application of these methods to OCT images is the presence of noise. The main noise sources in OCT images are shot noise originating from the light source and detection system, and speckle noise originating form interferometric detection of light scattered in optical media with random distribution of the refractive index. The influence of noise on segmentation results can be suppressed by numerical filtering and application of data averaging methods [I.B.2]. However, in most cases complete elimination of the noise, especially speckle noise, is difficult to achieve because it results in the degradation of axial and/or transverse imaging resolution, *i.e.* information about fine details of object structures is lost. However, if the goal is to approximate the curvature of the eye fundus in order to provide a reference surface for visualization of retinal and choroidal layers (as in the methods developed in my research projects), then the loss of information about small features does not influence the final result.

The application of gradient methods in the low-pass filtered images renders information about locations of the edges of all retinal layers. The challenge in segmentation of the OCT images is a correct identification of a selected anatomical layer. Typically, in OCT images the strongest gradient corresponds to the edges of the retinal pigment epithelium. However, other highly scattering layers (*e.g.* nerve fiber layer or retinal blood vessels) can generate gradients with values higher than the RPE. For most retinal OCT data (except of advanced stages of pathologies affecting the RPE, *e.g.* geographic atrophy) this situation is confined to a small collection of A-scans and can be considered as atypical. In the developed data processing techniques, I have applied statistical analysis of the strongest gradient location which enables estimation of the most probable position of the RPE edge in consecutive B-scans [I.B.1, I.B.4]. In the normal retina, this edge has a regular, continuous shape. However, development of pathologies often disrupts the shape of the RPE, and estimation of the "reference surface" requires fitting mathematical functions to the data points obtained in the initial segmentation. The most commonly used method is polynomial curves fitting in consecutive B-scans. However, this approach fails in case of substantial irregularities of the RPE edge shape and leads to large variations of the curvatures

in the lines fitted among neighboring B-scans (artifacts of the eye fundus curvature estimation). Better results can be obtained by estimating the fundus curvature with surfaces. In the developed methods, I have used for this purpose Zernike polynomials.

I have used data processing methods utilizing polynomial curve fitting for the visualization of pathological changes of the outer retina in selected ocular diseases, including age related macular degeneration [I.B.4]. I have demonstrated that *en face* projection imaging methods are well suited for visualization of pathology developing in the retinal pigment epithelium and in the photoreceptor layer (drusen, RPE atrophy, retinal detachments, photoreceptor cells damage, etc.) (Fig.1.). This type of visualization enabled classification of pathological changes characteristic of selected pathologies and their qualitative assessment. The project was a part of my postdoctoral scientific training. I have continued development of the layered visualization methods during my senior scientific training at Vision Science and Advanced Retinal Laboratory, University of California, Davis, USA. I have used methods with Zernike polynomials fitting for visualization of the vascular networks of the choroid [I.B.1]. In particular, *en face* visualization of the *choriocapillaris* was a foundation for further morphometric analysis.

b. Morphometric analysis of the *choricapillaris* layer.

The *en face* visualization of the retinal and choroidal layers not only enables qualitative analysis of the posterior eye segments vasculature, but also aids quantitative assessment of its selected morphological features [II.B.4]. The FDML ssOCT imaging of the eye fundus at 1.7 MHz A-scan rate renders data sets revealing the morphology of *choriocapillaris*, which opens new possibilities to analyze pathology development, especially in age related macular degeneration (AMD). In the development of quantitative data analysis methods for choriocapillaris layer, I took into account the known outcomes of the early AMD development:

- accumulation of waste materials of the visual processes within the Bruch's membrane and between the Bruch's membrane and RPE (different types of drusen, especially basal laminar deposits),
- *chriocapillaris* atrophy, which is preceded by changes in the structure of the *choriocapillaris* meshwork.

To enable the assessment of waste materials accumulation between the RPE and choriocapillaris, I have proposed mapping of the RPE-to-*choriocapillaris* distance. The analysis relays on identification of the RPE layer position in the intensity B-scans, and *choriocapillaris* layer location in the OCT angiography cross-sections. The RPE position is determined by finding locations of the intensity peaks exceeding an empirically set threshold, in subsequent mean axial intensity profiles. The mean intensity profiles are calculated by averaging subsets of A-scans within a rolling square window. The *choriocapillaris* position is determined by finding locations of the peaks closest to the RPE in mean OCT angiography axial profiles. The RPE-to-*choriocapillaris* positions are visualized in a form of *en face* maps (Fig.11.).

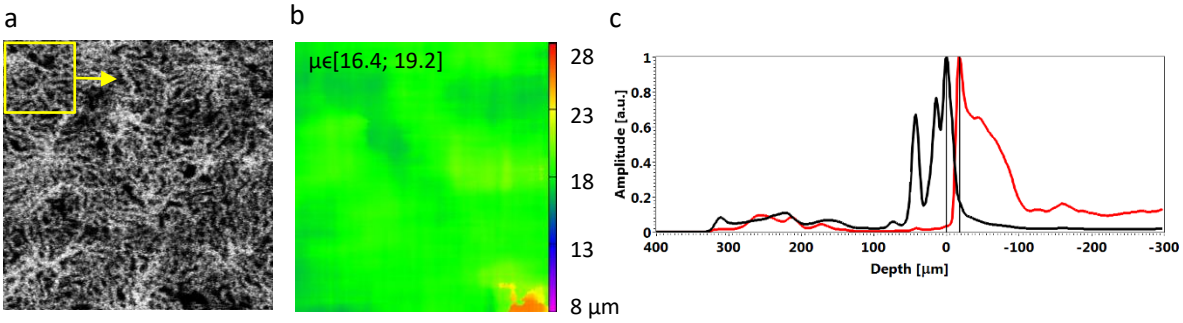

Fig. 11. Measurement of the distance between RPE and *choriocapillaris* layer. A. *En face* projection of the *choriocapillaris* layer in the foveal area of a healthy eye, the rectangle illustrates the window size used for the averaging of A-scans prior to analysis of the peaks positions, image size 1.2 mm^2. b. Map of the distances between RPE and *choriocapillaris*; the values given in the image are the limits of the 95% confidence interval of the mean value. c. Mean depth profiles of the intensity data (black) and OCT angiography data (red) obtained by averaging of all A-scans within three-dimensional data sets.

To enable the assessment of changes in the vascular morphology of *choriocapillaris*, I have developed data processing methods based on the analysis of radial power spectrum. The underlying assumption is that changes in the vascular structure can manifest as changes in the spatial power spectrum of the *choriocapillaris* images. The data processing includes computation of two-dimensional Fourier transform followed by radial averaging (averaging over full angular span for each radial location in the spatial power spectrum). To remove the frequency offset, similar calculations are performed in a set of depth locations in the OCTA images of the choroid. After subtraction of the frequency offset, a characteristic peak is visualized in the *choriocapillaris* radial power spectrum, which can be fitted with a Gaussian function (Fig.12).

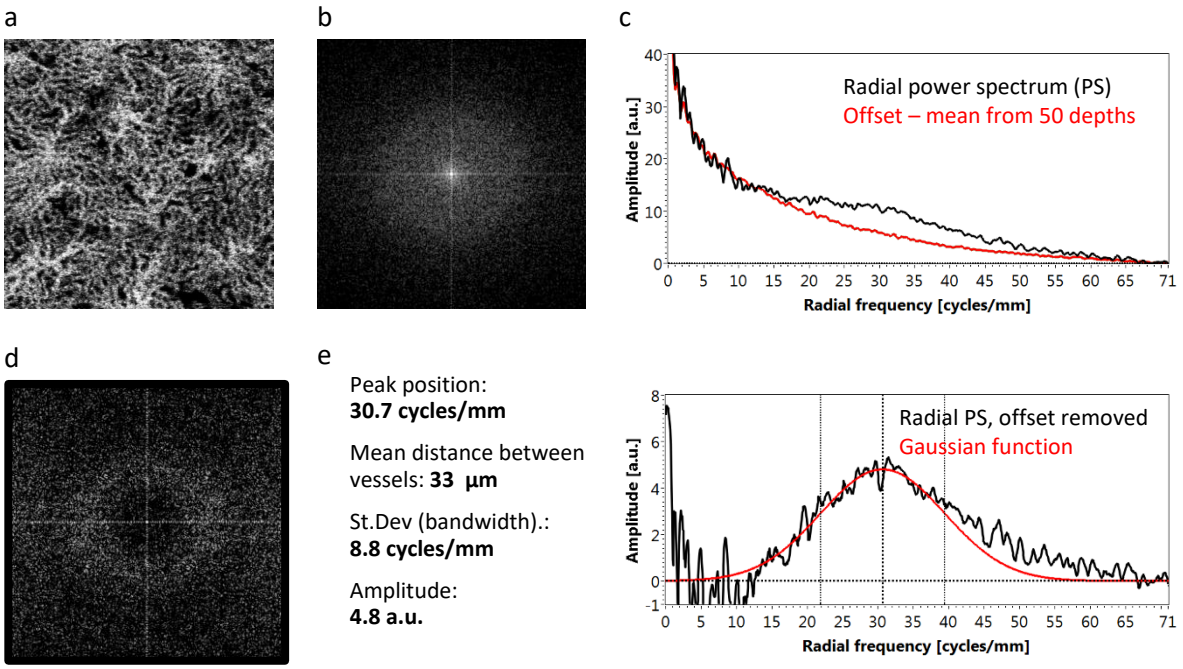

Fig. 12. Spatial power spectrum analysis of the *choriocapillaris* images. a. *En face* projection of *choriocapillaris* image obtained in the eye of a healthy volunteer. b. Spatial power spectrum. c. Radial power spectra of the *choriocapillaris* (black color) and mean radial power spectrum of the choroid (red color). d. Spatial power spectrum after offset removal. e. Radial power spectrum after offset removal (black color) and fitted Gaussian function (red color).

The peak position of the Gaussian function corresponds to the spatial frequency characteristic of *choriocapillaris* meshwork. The reciprocal of the characteristic spatial frequency corresponds

to the mean distance between vessels (inter-vessel distance). Standard deviation of the fitted Gaussian function can serve as a measure of spatial frequency bandwidth, and the amplitude can be used as a metric to characterize *choriocapillaris* structure visibility.

Yet another metric useful in quantitative analysis of the *choriocapillaris* layer is the flow fill factor defined as a proportion of the image area occupied by flow to the total scanned area of the object. The computation of the flow fill factor requires application of numerical morphological operators. In the first step, I have implemented image filtration with a spatial filter constructed based on the analysis of the *choriocapillaris* spatial frequency bandwidth. In the filtered *en face* projection image, I have applied morphological operations leading to skeletonization and binarization of the *choriocapillaris* (Fig.13.). The flow factor was then calculated as a ratio of the sum of the binarized image to the total number of image pixels. In addition, the binarized image can serve as a basis for further data analysis leading to generation of blood flow models of *choriocapillaris*.

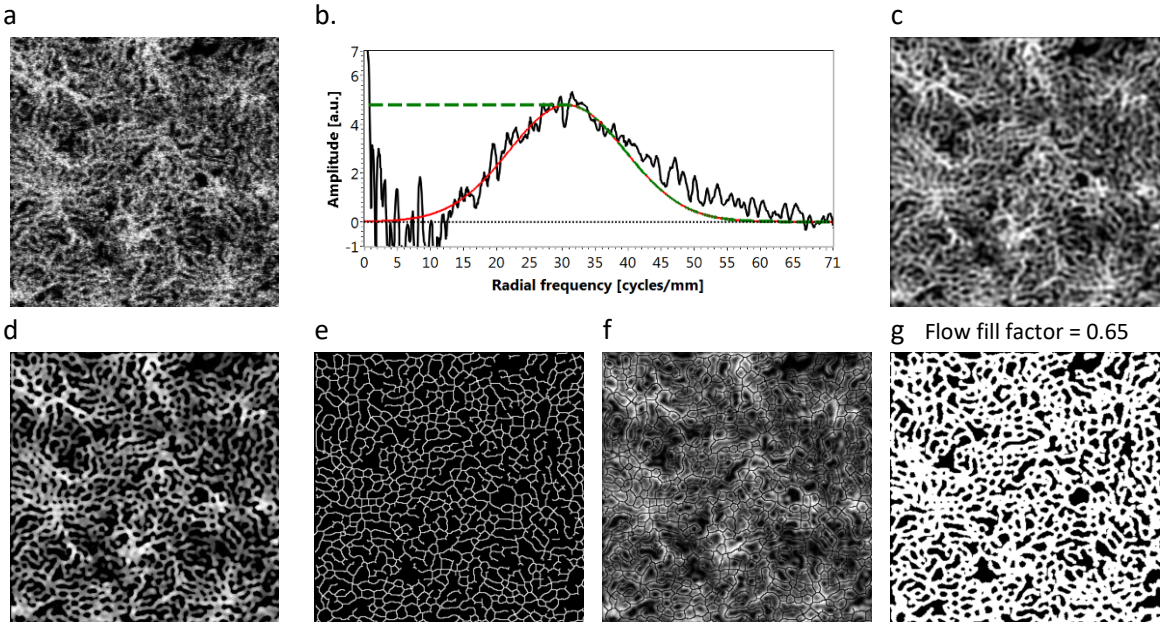

Fig. 13. Estimation of the flow fill factor. a. *En face* projection of the *choriocapillaris*. b. Construction of the filter function (green line) based on the radial power spectrum analysis. c. Filtered *choriocapillaris* image. d. Thresholding based on local intensity distribution. e. Result of skeletonization (morphological thinning operation). f. Overlay of the filtered *choriocapillaris* with the skeletonized image – skeleton indicates vessels centers. g. Binarized *choriocapillaris* image obtained by dilation of the skeleton based on local intensity analysis.

c. Reduction of motion artifacts and three-dimensional data averaging methods.

The usefulness of the OCT data in visualization of the posterior eye segment tissue and vasculature depends on the images quality and level of captured details. Increasing imaging speed is crucial in OCT techniques because it shortens data acquisition time and decreases the number of motion artifacts. However, complete elimination of motion artifacts is not possible. In most cases the OCT data contains discontinuities in the imaged tissue structures connected to saccadic motion of the eye, and less evident distortions connected to eye drifts. In OCT angiography and velocimetry, the eye motion is a source of a false flow signal obstructing the information about blood flow in the areas where the motion occurred during the scanning of the retina. This type of artifacts can cause loss of diagnostically important

information, hinder interpretation of the images and impede their quantitative analysis. In particular, motion artifacts can cause errors in segmentation methods of the retinal and choroidal layers.
The two methods for reduction of motion artifacts in OCT are:

a) tracking of the eye motion and correction of the scanning beam position in real time [111-114],
b) correction of the motion artifacts in the acquired data sets using numerical methods [11, 115-122].

As a part of realization of research projects on high speed OCT imaging, I have developed a method for reduction of motion artifacts in post-processing (in the acquired volumetric data sets) [I.B.1]. The method uses layered data visualization described in the previous sections. The goal is to correct motion artifacts connected to saccadic motion of the eye. Artifacts caused by eye drifts are ignored. The simplifying assumption is that between the saccadic motions, sections of the three-dimensional data sets behave like rigid objects and their position can be corrected by translations. This assumption is approximately correct if the imaging is sufficiently fast (~100 000 A-scans/s or faster) and the imaged volunteer has no difficulties with focusing the gaze on a fixation mark. Implementation of the method requires acquisition of a few (5 or more) three-dimensional data sets from the same location in the retia, which are then processed to generate standard structural and angiographic B-scans. Application of the layered visualization methods results in the *en face* images of the retinal vasculature. Motion artifacts are easily identifiable in the angiographic *en face* projections as horizontal lines with a false, maximum flow signal. Positions of these artifacts are used to break the original projection images and three-dimensional data sets into smaller, saccadic motion free segments. In the same time, a matrix mapping original locations of the segments in the *en face* projection images is created. In the next step a matrix mapping corrected locations of the segments is generated. The procedure starts with a selection of two largest and most overlapping segments from two different data sets. Their relative position is corrected by correlation of their angiographic *en face* projections, and the images are averaged to serve as a reference for the "next" segment. The "next" segment is the largest, and having the largest overlap with the reference image among the remaining segments. The position of the "next" segment is corrected by correlation with the reference. The procedure is repeated until the collection of segments is exhausted. The result is a matrix of transverse locations of all segments in the final three-dimensional data sets. To correct for the axial translations, B-scans of overlapping segments are correlated. In the last step, corrected for transverse and axial motions segments are averaged to render the final averaged three-dimensional data set, which can be used for further data analysis. In my projects, I have used the averaged three-dimensional data sets for improved visualization of the retinal and choroidal vasculature, and for segmentation of the retinal vascular networks which resulted in generation of a skeletonized vascular model (Fig.7.).

4.6. RECAPITULATION

In my research summary, I have presented a series of research projects which led to development of experimental and data processing methods for high speed, *in vivo* imaging of the human posterior eye segment with Fourier domain optical coherence tomography techniques. The outcome of the projects realization were four generations of OCT systems used for imaging of the tissue and vasculature of the eye fundus. The first-generation OCT systems (spectral domain OCT with imaging speeds of 25 000 A-scans/s) enabled imaging of the retinal tissue morphology and development of three-dimensional data visualization methods facilitating the assessment of ocular pathologies. The second-generation systems

(spectral domain OCT with imaging speeds of 100 000 – 300 000 A-scans/s) improved the quality of the acquired data and enabled visualization tissue morphology details down to the cone photoreceptor cells in the eyes of healthy volunteers, without the application of adaptive optics techniques. More importantly, they enabled observation of dynamic processes: tracking three-dimensional eye motions over time, detection of the OCT signal variations caused by blood flow, and measurement of the axial component of the flow velocity in the retinal vasculature down to the capillary vessels. The third-generation systems (swept source OCT operating at 1050 nm center wavelength, with imaging speeds of 100 000 A-scans/s) enabled increased imaging depth, three-dimensional visualization of the retinal vasculature, and detection of the blood flow in the *choriocapillaris* with OCT angiography methods. The fourth-generation systems (FDML ssOCT at 1050 nm, operating at 1.7 MHz A-scan rate) enabled a break-through in imaging of the human choroid *in vivo*. For the first time, it was possible to image deep choroidal vessels (Sattler's and Haller's layers) with the OCT angiography methods, visualize *choriocapillaris* layer morphology and develop quantitative methods for the analysis of *choriocapillaris* morphology. In addition, axial flow velocity component measurement became feasible in selected choroidal vessels in the slow flow detection regime (axial flow velocity values of a fraction of mm/s), and in the deep vessels delivering blood to the choroid (axial flow velocity values larger than 50 mmm/s).
The realization of my research projects included all stages of the scientific workflow: selection of research topics and methodology, planning and design the experiments, design and construction of the experimental setups, performing the experiments (including imaging of patients in ophthalmology clinics), development of data analysis methods and their implementations.
The outcomes of the research projects were: publications, presentations at international conferences, prototype OCT setups used for patients imaging in the ophthalmology clinics, and commercialization of the research results [III.A.1-4].

5. SUMMARY OF OTHER SCIENTIFIC ACHIEVEMENTS

5.1. DEVELOPMENT OF IMAGING METHODS FOR OPTHTHALMIC APPLICATIONS

5.1.1. Application of active eye tracking methods in structural OCT imaging and OCT angiography [II.B.5, II.H.26, II.H.29].

Increasing speed in OCT imaging is one of the most important goals enabling *in vivo* imaging of the eye tissues morphology down to the photoreceptor cell levels, and dynamical processes connected to tissue functioning. However, it does not eliminate motion artifacts in the registered images. One of the methods for motion artifact reduction is application of real time eye tracking and motion compensation techniques. It requires construction of experimental setups enabling fast imaging of the eye fundus, automatic detection of the motion direction and magnitude, and providing a feed-back to the OCT imaging system, i.e. application of the measured motion vectors for the compensation of eye motions.

In my research projects, I have used a tracking scanning laser ophthalmoscope (TSLO) designed in Roorda Labs, Univeristy of California, Berkeley, USA [113, 114, 123], and constructed in Vision Science and Advanced Retinal Imaging Laboratory, University of California, Davis, USA. The device was optically and electronically coupled with a swept source OCT system (100 kHz A-scan repetition rate). The eye motion compensation was achieved by application of correction signals generated by the TSLO system, to the OCT optical scanners, which defflected the OCT beam in order to follow the new position of the imaged eye fundus area. The aim of the research project was application of active eye tracking

technique for motion correctin in OCT angiography imaging. The experiments have demonstrated that despite the improvement of the structural imaging quality, active eye tracking techniques introduce noise in the OCT angiography data. Even small errors in the OCT beam position correction caused by errors in the eye tracking, result in OCT signal decorrelation and increase OCTA noise or introduce imaging artifacts. As a consequence the active eye tracking methods may decrease the quality of imaging in OCT angiography instead of facilitating their improvement. The main outcome of the project was recognition of the need for development of new methods of eye tracking, maintaining low OCT signal decorrelation noise. My role in the project included planning and performing the experiments, development and implementation of the OCT angiography data processing methods, and data analysis.

5.1.2. Application of adaptive optics techniques for morphometric analysis of the photoreceptor cells layer in OCT imaging [II.A.28, II.H.27].

The transverse imaging resolution of optical systems is determined by their numerical aperture. The higher is the numerical aperture, the better is the transverse imaging resolution. However, in ophthalmic applications of the OCT techniques the numerical aperture is given by the imaging system which includes the eye. In this case, increasing the numerical aperture requires increasing the beam spot size at the cornea, which in turn necessitates dilation the eye pupil. However, application of light beams with spot diameters larger than ~3 mm (at the cornea) decreases the transverse imaging resolution instead of improving it, due to aberrations of the eye. Standard ophthalmic OCT setups can achieve transverse imaging resolution of ~7-10 µm in the eyes with low aberrations. Higher imaging resolutions can be achieved by application of adaptive optics techniques.

During my scientific training at Vision Science and Advanced Retinal Imaging Laboratory, University of Davis, California, I participated in a research project on OCT imaging of the photoreceptor cells layer with the real-time correction of eye aberrations [124]. In this technique, the aberrations are analyzed using a Shack-Hartman wavefront sensor. The correction is performed with a deformable mirror optically and electronically coupled with the wavefront sensor. The aim of the project was analysis of the photoreceptor cells layer morphology in neurodegenerative retinal diseases (*e.g.* age related macular degeneration). The goals were to develop methods for morphometric analysis of single cone photoreceptor cells, and identification of the origins of the four distinct scattering bands within the photoreceptor-RPE complex, observed in the OCT cross-sectional images. My role in the project was solving technical problems connected to the AO-OCT imaging system, development of the experimental methods and performing of the experiments.

5.1.3. Application of spectral domain OCT for imaging of the anterior chamber of the eye [II.A.10, II.A.19, II.A.20, II.B.23, II.B.26].

The ophthalmic applications of the spectral domain OCT technique include not only imaging of the posterior eye segment but also imaging of the anterior chamber of the eye. The main challenge in this application of sdOCT was development of experimental methods enabling wide field imaging (>~10 mm) and large depth of view (a few millimeters). Once more, achieving wide field of view required development of high speed OCT systems (~100 000 A-scans/s or more). Increasing the imaging depth required design and construction of OCT spectrometers with high spectral imaging resolutions, to enable detection of high frequency interference fringes. My involvement in the research projects included design and construction of OCT setups, performing the experiments (including imaging of patients) and data analysis. The imaging systems and developed experimental methods were used for imaging of diseases developing in the anterior chamber of the eye and for tests of contact lens fitting.

5.2. DEVELOPMENT OF OPTICAL COHERENCE MICROSCOPY METHODS

5.2.1. Imaging of the vascular networks in small animal brains and analysis of neuro-vascular coupling [II.A.1, II.A.3-5 , II.A.9].

In addition to ophthalmic applications, the OCT techniques have found numerous applications in other biomedical research fields. One of them is *in vivo* microscopy imaging of brain tissue in anesthetized animals, *e.g.* rodents. The goal of this research is better understanding of the mechanisms influencing blood circulation, blood oxygenation, and the mechanisms of neuro-vascular coupling in the brain with normal function and influenced by factors disrupting the neural activity (*e.g.* strokes). The OCT technique can provide information about functional processes occurring in the outer layers of the brain tissue up to ~1 mm depth, *i.e*. is suitable for the analysis of the cerebral cortex. Application of OCT angiography methods enables mapping the blood flow in the vascular networks and its changes caused by injury. OCT velocimetry methods can provide quantitative information about flow velocity. Analysis of the spectrum of light scattered in selected blood vessels or tissues, *i.e.* spectroscopic OCT analysis, can enable measurement of the hematocrit as well as blood and tissue oxygenation.

During my postdoctoral training, I participated in the research on neuro-vascular coupling in the rodents' cerebral cortex. The project was realized in cooperation with Photon Migration Laboratory, Martinos Center Biomedical Imaging, Massachussetts General Hospital, Harvard Medical School, Boston, MA, USA. My role in the projects included design and construction of the experimental setup for optical coherence microscopy imaging in combination with two-photon microscopy system. During my employment at Medical Physics Group, Institute of Physics, N. Copernicus University, Poland, I participated in the research on imaging of the vascular networks in the cerebral cortex of mice, and changes in blood perfusion caused by strokes. My role in this project included design and construction of one of the imaging systems, planning of the experiments, and consultation of the experimental procedures and their outcomes.

5.2.2. Doppler OCT analysis of morphotic elements of blood [II.B.12, III.A.1].

One of the effects of blood flow in vascular networks localized within tissues with high light scattering is generation of flow projections. Light propagating through the vascular networks is partially forward-scattered at the moving blood cells. This effect generates time-fluctuations of the registered complex amplitudes. In OCT angiography and Doppler OCT images the fluctuations manifest as false flow signal observed in highly scattering tissues underlying the blood vessels, *i.e.* they manifest as flow projections in the static tissues [125]. Due to a random character of the blood cells flow, the flow projections have random distribution of the complex amplitude in the transverse and depth direction of the imaged object. However, their statistical properties (*e.g.* standard deviation, mean speckle size, phase distribution) depend on the scattering properties of the blood cells and are characteristic of specific morphotic elements. This observation was a foundation for the development of methods for identification of selected blood cells (erythrocytes and leukocytes) by statistical analysis of the flow projections.

My involvement in this research was connected to a joint project between a AM2M spin-off company, of which I am a co-founder, and CORMAY company which specializes in development agents for medical analytical diagnostics. My role was supervision of the project realization, planning of the experiments, interpretation of the results, development of data analysis methods, consultations of the experimental procedures.

5.2.3. Development of OCT microscopy detection methods of neural activity in insect models [II.B.7, II.B.9].

In Fourier domain OCT imaging, the information about the object is obtained by analysis of the registered spectral interference signal. In structural OCT imaging, the information about tissue morphology is encoded in the changes of the light intensity scattered at subsequent layers, and manifests as changes in the depth modulation of the interference fringe pattern across the depth and breadth of the object. In addition to structural imaging, OCT techniques also enable detection of the functioning of the living tissues. This information is obtained by analysis of the OCT signal changes caused by physiological processes influencing the tissue morphology or its optical properties. In particular, the activity of neural tissue causes migration of the water molecules and ions participating in the propagation of action potentials, which can cause changes in the cells volume and tissue refractive index. Due to light scattered at active neural tissue, subtle changes in the intensity, frequency (visible as phase change of the fringe pattern), can be observed in the registered OCT signal. Development of methods for detection of biological tissues activity was one of the aims of the research project entitled: "Development of neural tissue activity detection methods with Fourier domain OCT", in which I was a principal investigator. The aim of the project was to study the influence of the neural tissue activity on the registered OCT signal. The research was performed in neural cords isolated from American cockroach. The outcome of the project realization was construction of the OCT setup for structural and functional imaging of tissue samples, demonstration of the possibility to image the connectives of the neural cord at a cellular level, development of experimental and data processing methods enabling detection of the neural activity in the connectives, in correlation with electrophysiology. The project was realized in collaboration with the Biophysics Department, Faculty of Biology and Earth Sciences, N. Copernicus University, Poland. My role in this project was obtaining funding for project realization, leading the research, design and construction of the experimental setups, planning and conducting the experiments, development of the data analysis methods.

5.3. APPLICATION OF OCT TECHNIQUE IN ART CONSERVATION STUDIES [II.A.17, II.B.21, II.B.22].

The main application of OCT techniques is in biomedical sciences. However, they are also successfully used in the imaging of the non-biological objects. For example, OCT techniques can be applied for the imaging of the artworks, as a tool aiding the art restoration and conservation process, or in historical art studies. As in biomedical imaging, imaging of artworks requires application of non-destructive methods and techniques enabling analysis of three-dimensional or layered structures of the studied objects. However, the experimental methods must be adjusted to specific requirements imposed by the examined artwork. Especially, spectral bandwidths of light emitted by sources used in the imaging setups must be adjusted depending on the optical properties of the materials used for the creation of artworks.

During my postdoctoral training, I was participating in a study of renaissance easel and panel paintings with OCT technique [II.A.17]. The imaging was performer with an FDML swept source OCT system operating at 1300 nm center wavelength. The imaging platform was adjusted to enable imaging of paintings mounted on easels. The aim of the study was analysis of the underdrawings located underneath layers of vernix and paint, and profilometry analysis of gold punchwork in panel paintings. The study was performed in collaboration with Harvard University Art Museums, Harvard University, Cambridge, MA, USA. My role in the projects realization included performing of the experiments, development and application of data analysis methods, and data processing.

I Gorczynska

Applicant's signature

6. REFERENCES

Legend:

I.B. – publications selected for presentation of the scientific achievements,

II.A. – other authored works published in Journal Citation Reports (JRC) data base,

II.B. – authored works published in journals not listed in JRC data base,

II.H. – conference talks and lectures,

III.A. – commercialization of research.

List of the above mention works is included in appendix 4.

Other works cited in the summary of the scientific achevements.

1. D. Huang, et al., Science **254**(5035), 1178-1181 (1991).
2. A. F. Fercher, et al., American journal of ophthalmology **116**(1), 113-114 (1993).
3. E. A. Swanson, et al., Opt Lett **18**(21), 1864-1866 (1993).
4. J. Fujimoto, et al., Investigative Ophthalmology & Visual Science **57**(9), OCT1-OCT13 (2016).
5. K. Bizheva, et al., PNAS **103**(13), 5066-5071 (2006).
6. V. J. Srinivasan, et al., Optics Letters **31**(15), 2308-2310 (2006).
7. V. J. Srinivasan, et al., Optics Express **17**(5), 3861-3877 (2009).
8. R. S. Jonnal, et al., Optics Express **18**(5), 5257-5270 (2010).
9. T. Schmoll, et al., J. Biomed. Opt. **15**(4), 041513-041513-041518 (2010).
10. M. Pircher, et al., Biomedical Optics Express **2**(1), 100-112 (2011).
11. R. S. Jonnal, et al., Biomedical Optics Express **3**(1), 104-124 (2012).
12. E. Wei, et al., Plos One **8**(12), e81343 (2013).
13. H. Spahr, et al., Optics Letters **40**(20), 4771-4774 (2015).
14. M. M. Teussink, et al., Biomedical Optics Express **6**(5), 1632-1647 (2015).
15. D. Hillmann, et al., PNAS **113**(46), 13138-13143 (2016).
16. O. P. Kocaoglu, et al., Biomedical Optics Express **7**(11), 4554-4568 (2016).
17. S. Yazdanfar, et al., Optics Letters **25**(19), 1448-1450 (2000).
18. R. A. Leitgeb, et al., Optics Express **11**(23), 3116-3121 (2003).
19. B. R. White, et al., Optics Express **11**(25), 3490-3497 (2003).
20. L. Wang, et al., Opt. Comm. **242**(4–6), 345-350 (2004).
21. A. H. Bachmann, et al., Opt. Express **15**(2), 408-422 (2007).
22. Y. Wang, et al., J. Biomed. Opt. **12**(4), 041215-041215-041218 (2007).
23. A. Szkulmowska, et al., Opt. Lett. **33**(13), 1425-1427 (2008).
24. M. Szkulmowski, et al., Opt. Express **16**(9), 6008-6025 (2008).
25. Y. Wang, et al., J. Biomed. Opt. **13**(6), 064003-064003-064009 (2008).
26. T. Schmoll, et al., Optics Express **17**(5), 4166-4176 (2009).
27. A. Szkulmowska, et al., Opt. Express **17**(13), 10584-10598 (2009).
28. Y. K. Tao, et al., Optics Express **17**(5), 4177-4188 (2009).
29. B. Baumann, et al., Biomedical Optics Express **2**(6), 1539-1552 (2011).
30. B. Braaf, et al., Opt. Express **19**(21), 20886-20903 (2011).
31. H. C. Hendargo, et al., Biomed. Opt. Express **2**(8), 2175-2188 (2011).
32. W. Choi, et al., Biomedical Optics Express **3**(5), 1047-1061 (2012).
33. M. Miura, et al., Investigative Ophthalmology & Visual Science **53**(11), 7137-7141 (2012).
34. V. Doblhoff-Dier, et al., Biomedical Optics Express **5**(2), 630-642 (2014).
35. R. Haindl, et al., Biomedical Optics Express **7**(2), 287-301 (2016).
36. R. Leitgeb, et al., in *Conference on Coherence Domain Optical Methods in Biomedical Science and Clinical Applications V*, V. Tuchin, ed. (San Jose, Ca, 2001), pp. 123-127.
37. D. J. Faber, et al., Optics Letters **28**(16), 1436-1438 (2003).
38. C. Xu, et al., Appl. Opt. **44**(10), 1813-1822 (2005).
39. F. Robles, et al., Optics Express **17**(8), 6799-6812 (2009).
40. S. Chen, et al., Biomedical Optics Express **6**(8), 2840-2853 (2015).
41. J. Yi, et al., Light Sci Appl **4**e334 (2015).
42. C. W. Merkle, et al., Biomedical Optics Express **7**(10), 4289-4312 (2016).
43. S. Chen, et al., Biomedical Optics Express **8**(3), 1415-1429 (2017).
44. D. Koozekanani, et al., IEEE Transactions on Medical Imaging **20**(9), 900-916 (2001).
45. D. Cabrera Fernández, et al., Optics Express **13**(25), 10200-10216 (2005).
46. H. Ishikawa, et al., Investigative Ophthalmology & Visual Science **46**(6), 2012-2017 (2005).
47. M. Mujat, et al., Optics Express **13**(23), 9480-9491 (2005).

48. M. Szkulmowski, et al., J. Biomed. Opt. **12**(4), 041207-041207-041211 (2007).
49. T. Fabritius, et al., Optics Express **17**(18), 15659-15669 (2009).
50. M. K. Garvin, et al., IEEE Transactions on Medical Imaging **28**(9), 1436-1447 (2009).
51. A. Mishra, et al., Optics Express **17**(26), 23719-23728 (2009).
52. S. J. Chiu, et al., Optics Express **18**(18), 19413-19428 (2010).
53. M. A. Mayer, et al., Biomedical Optics Express **1**(5), 1358-1383 (2010).
54. H. Zhu, et al., Optics Express **18**(24), 24595-24610 (2010).
55. A. S. G. Singh, et al., Biomedical Optics Express **2**(5), 1328-1339 (2011).
56. K. A. Vermeer, et al., Biomedical Optics Express **2**(6), 1743-1756 (2011).
57. L. Duan, et al., Optics Express **20**(3), 3353-3366 (2012).
58. T. Torzicky, et al., Optics Express **20**(7), 7564-7574 (2012).
59. V. Kajic, et al., Biomed. Opt. Express **4**(1), 134-150 (2013).
60. A. Lang, et al., Biomedical Optics Express **4**(7), 1133-1152 (2013).
61. A. Carass, et al., Biomedical Optics Express **5**(4), 1062-1074 (2014).
62. D. Kaba, et al., Optics Express **23**(6), 7366-7384 (2015).
63. Z. Chu, et al., J. Biomed. Opt. **21**(6), 066008-066008 (2016).
64. S. B. Ploner, et al., Retina **36** Suppl 1S118-S126 (2016).
65. K. Kurokawa, et al., Biomedical Optics Express **8**(3), 1803-1822 (2017).
66. S. Makita, et al., Opt. Express **14**(17), 7821-7840 (2006).
67. R. K. Wang, et al., Opt. Express **15**(7), 4083-4097 (2007).
68. L. An, et al., Opt. Express **16**(15), 11438-11452 (2008).
69. A. Mariampillai, et al., Opt. Lett. **33**(13), 1530-1532 (2008).
70. J. Fingler, et al., Opt. Express **17**(24), 22190-22200 (2009).
71. L. An, et al., J. Biomed. Opt. **15**(2), 026011-026011-026019 (2010).
72. A. Mariampillai, et al., Opt. Lett. **35**(8), 1257-1259 (2010).
73. R. K. Wang, et al., Opt. Lett. **35**(9), 1467-1469 (2010).
74. L. Yu, et al., J. Biomed. Opt. **15**(1), 016029-016029-016024 (2010).
75. C. Blatter, et al., J. Biomed. Opt. **17**(7), 070505 (2012).
76. B. Braaf, et al., Opt. Express **20**(18), 20516-20534 (2012).
77. Y. L. Jia, et al., Opt. Express **20**(4), 4710-4725 (2012).
78. K. Kurokawa, et al., Opt. Express **20**(20), 22796-22812 (2012).
79. W. Choi, et al., Plos One **8**(12), (2013).
80. D. Y. Kim, et al., PNAS **110**(35), 14354-14359 (2013).
81. M. S. Mahmud, et al., J. Biomed. Opt. **18**(5), 050901 (2013).
82. R. Poddar, et al., J. Biomed. Opt. **19**(12), 126010-126010 (2014).
83. D. M. Schwartz, et al., Ophthalmology **121**(1), 180-187 (2014).
84. N. Uribe-Patarroyo, et al., Opt. Express **22**(20), 24411-24429 (2014).
85. S. S. Gao, et al., Opt. Lett. **40**(10), 2305-2308 (2015).
86. A. Lozzi, et al., Biomed. Opt. Express **6**(7), 2435-2447 (2015).
87. D. Ruminski, et al., Biomed. Opt. Express **6**(8), 2738-2754 (2015).
88. A. Zhang, et al., J. Biomed. Opt. **20**(10), 100901-100901 (2015).
89. S. Makita, et al., Biomedical Optics Express **7**(4), 1525-1548 (2016).
90. A. F. Fercher, et al., Opt Commun **117**(1-2), 43-48 (1995).
91. G. Ha¨usler, et al., J. Biomed. Opt. **3**(1), 21-31 (1998).
92. M. Wojtkowski, et al., J. Biomed. Opt. **7**(3), 457-463 (2002).
93. S. R. Chinn, et al., Optics Letters **22**(5), 340-342 (1997).
94. B. Golubovic, et al., Optics Letters **22**(22), 1704-1706 (1997).
95. F. Lexer, et al., Appl. Opt. **36**(25), 6548-6553 (1997).
96. Y. K. Tao, et al., Opt. Express **16**(16), 12350-12361 (2008).
97. J. A. Izatt, et al., Optics Letters **22**(18), 1439-1441 (1997).
98. T. G. van Leeuwen, et al., Optics Letters **24**(22), 1584-1586 (1999).
99. V. X. D. Yang, et al., Opt Commun **208**(4–6), 209-214 (2002).
100. S. Yazdanfar, et al., Archives of Ophthalmology **121**(2), 235-239 (2003).
101. J. Tokayer, et al., Biomed. Opt. Express **4**(10), 1909-1924 (2013).
102. W. J. Choi, et al., Biomedical Optics Express **7**(7), 2709-2728 (2016).
103. Y. Zhao, et al., Optics Letters **25**(18), 1358-1360 (2000).
104. H. Ren, et al., Optics Letters **27**(6), 409-411 (2002).
105. D. Piao, et al., Optics Letters **28**(13), 1120-1122 (2003).
106. S. G. Proskurin, et al., Optics Letters **28**(14), 1227-1229 (2003).

107. A. Bouwens, et al., Optics Express **21**(15), 17711-17729 (2013).
108. N. Uribe-Patarroyo, et al., Physical Review E **94**(2), 022604 (2016).
109. J. Fingler, et al., Opt. Express **15**(20), 12636-12653 (2007).
110. F. Jaillon, et al., Opt. Express **20**(1), 385-396 (2012).
111. R. D. Ferguson, et al., Optics Letters **29**(18), 2139-2141 (2004).
112. D. X. Hammer, et al., J. Biomed. Opt. **10**(2), 024038-02403811 (2005).
113. K. V. Vienola, et al., Biomed. Opt. Express **3**(11), 2950-2963 (2012).
114. B. Braaf, et al., Biomed. Opt. Express **4**(1), 51-65 (2013).
115. S. Ricco, et al., in *Medical image computing and computer-assisted intervention : MICCAI*(2009), pp. 100-107.
116. O. P. Kocaoglu, et al., Biomedical Optics Express **2**(4), 748-763 (2011).
117. M. F. Kraus, et al., Biomed. Opt. Express **3**(6), 1182-1199 (2012).
118. H. C. Hendargo, et al., Biomed. Opt. Express **4**(6), 803-821 (2013).
119. M. F. Kraus, et al., Biomedical Optics Express **5**(8), 2591-2613 (2014).
120. Y. Wang, et al., Biomedical Optics Express **6**(11), 4302-4316 (2015).
121. P. Zang, et al., Biomedical Optics Express **7**(7), 2823-2836 (2016).
122. M. Heisler, et al., J. Biomed. Opt. **22**(3), 036007-036007 (2017).
123. C. K. Sheehy, et al., Biomed. Opt. Express **3**(10), 2611-2622 (2012).
124. R. J. Zawadzki, et al., Biomedical Optics Express **2**(6), 1674-1686 (2011).
125. P. Ossowski, et al., Opt. Express **23**(21), 27724-27738 (2015).
126. W. S. Rasband, "ImageJ," (U. S. National Institutes of Health, Bethesda, Maryland, USA, 1997-2015).
127. J. Ahrens, et al., ParaView: an end-user tool for large data visualization, visualization handbook (Elsevier, 2005).

I Gorczyńska
Applicant's signature